Enhanced finite element formulation incorporating stress jumps and interface behaviour in structures with embedded linear inclusions

Francesco Riccardi, Cédric Giry, Fabrice Gatuingt

Enhanced finite element formulation incorporating stress jumps and interface behaviour in structures with embedded linear inclusions

Francesco Riccardi, Cédric Giry, Fabrice Gatuingt
LMT (ENS Paris-Saclay, CNRS, Universit Paris Saclay)

Abstract

When linear inclusions are embedded into a matrix, a perturbation is introduced in the boundary value problem written at the macroscale. Such inhomogeneity can provoke sharp gradients in the solution and a correct evaluation of the interface stress state reveals necessary when localised material degradations can lead to global failure mechanisms. In order to account for such refined description in large scale structural problems, a novel enhanced implicit finite element formulation is presented. The standard displacement approximation is improved by means of a kinematic enrichment aimed at reproducing the local interaction between the matrix and the inclusion. The microscale interface behaviour can then be directly evaluated from the stress jump arising in the bulk. From a computational point of view, this translates in solving an additional local equilibrium equation. The static boundary conditions at the inclusion ends are thus exactly verified and a good precision is achieved with minimal meshing effort and code modifications. The proposed model is applied to elementary and structural examples involving singularities and it is compared to other modelling strategies with focus both on global and local quantities as well on the convergence properties and corresponding CPU times of the approximated solution. *Keywords :* Embedded linear inclusions, Enhanced finite elements, Interface behaviour, Stress jump

1 Introduction

For several decades, matrix-inclusion problems have been object of extensive research in continuum mechanics [1, 2, 3, 4, 5, 6]. The case of linear inclusions has especially taken on great importance due to the wide range of engineering applications [7]. Among them we recall, for instance, the case of fibre-reinforced materials and the broad variety of structures with embedded reinforcements, namely rebars and anchors. The latter class ranges from the most common construction material, i.e. reinforced concrete, to the case of pile-raft foundations in civil engineering structures. Each specific problem is associated to one or more scales of observation and differs for the quantities of interest, while the common denominator is the fact that the cross sectional dimension of the inclusions is much smaller compared to the other characteristic lengths [8]. The multiscale nature underlying this set of problems thereby governs the choice of suitable modelling strategies, especially the reinforcement architecture, i.e. its geometry, volume, orientation and packing arrangement as well as the applied loading and boundary conditions must be attentively analysed in the process.

Understanding how the specific inclusion interacts with the surrounding material is an essential element for determining what level of accuracy is required in simulations. When such interaction tends to be highly localised, the onset of singular behaviours in the local stress distribution may require the explicit modelling of interfaces. This situation is encountered in a number of practical applications involving, for instance, the seismic retrofit of reinforced concrete structures by means of Externally Bonded (EB) and Near Surface Mounted (NSM) reinforcements [9, 10, 11, 12]. Due to their use in small portions of the structure, the performances of retrofitting procedures crucially depends on the effectiveness of the stress transfert between the reinforcements and the underlying material. For enhancing their behaviour, anchoring systems of limited extension and unaligned orientation are therefore embedded into concrete [13, 14, 15, 16, 17]. Under these circumstances, compatibility is enforced along the inclusion length whereas concentrated forces and moments are applied at the extremities. The high stress gradients resulting from this configuration, may induce the local failure of the strengthening component and compromise the safety of the entire structure [18, 19, 20]. Simple stiffness-based computations of similar problems by means of traditional macroscopic approaches may be insufficient from a reliability point of view and more refined stress analysis are thereby required for evaluating the onset of early ruptures or debonding mechanisms.

Some analytical solutions have shown, indeed, that linear stiffeners embedded in (semi-)infinite elastic media with loads applied at the inclusion ends induce jumps in the stress distribution and singularities at the extremities [1, 3]. Reproducing gradients and singularities in numerical solutions is still nowadays one of the major challenges in computational mechanics of civil engineering structures. For this purpose, Contrafatto *et al.* [21] developed a macro beam element with a single uniform reinforcement presented in the framework of the Strong Discontinuity Approach (SDA) [22, 23, 24, 25] for improving the description of unidimensional shear-lag

problems associated with pull-out configurations. Both concrete cracking and bond-slip effects between concrete and reinforcements are taken into account. In order to avoid excessively refined meshes, new enriching shape functions have also been proposed. In particular, polynomials, problem-oriented exponentials and B-splines have been compared. It is shown that the standard linear interpolation leads to large errors in the solution, whereas the results given by higher order approximations are significantly improved both at the global and the local level.

In large three-dimensional problems, as often occurs in civil engineering, the need to account for punctual material interactions and interface behaviours can easily become computationally prohibitive. Finite element implementations of multiscale approaches and 1D/2D structural theories have therefore been privileged in case of traditional reinforcement layouts. In the framework of mixing theories, Car *et al.* [26] have proposed a generalised model for describing the behaviour of long fibre-reinforced laminates. The composite material is here modeled in large strain settings as the compound of different phases homogeneously distributed in the volume (or in one of its portions) and contributing to the overall behaviour proportionally to their volume fraction. The assumed iso-strain hypothesis for enforcing compatibility between the compounding materials is then enhanced by considering anisotropic elastoplastic constituive laws for the phases. In the same context, a serial-parallel approach was proposed by Rastellini *et al.* [27] where the closure equations of the problem now consist in the association of the iso-strain hypothesis in the fibre direction with an iso-stress condition in the transversal direction. An application of this model has been presented by Martinez *et al.* [28] where the behaviour of reinforced concrete structures strengthened with Fibre Reinforced Polymers (FRP) is simulated.

In the context of computational homogenisation, Sciegaj *et al.* [29] have studied bond-slip mechanisms occurring in reinforced concrete by means of the FE^2 approach. Under the scale separation assumption, a two-scale model has been developed. The macroscale response is herein computed by averaging the subscale solution obtained from the resolution of an auxiliary problem formulated on the RVE. In particular, in the spirit of the Variational Multiscale Method (VMS) [30], the local displacement field is additively decomposed into a unique macroscopic (smooth) part and a fluctuation term which depends on the microscopic space variable only. Bond-slip behaviours are therefore computed on the RVE problem, where an appropriate choice of the Dirichlet and Neumann boundary conditions is essential for obtaining meaningful results.

An effective alternative to traditional homogenisation is represented by the multiphase model developed for inclusion-reinforced geostructures [8, 31, 32, 33]. The matrix and the reinforcements are in this case spatially superposed and in mutual equilibrium with the applied boundary conditions and the exchanged interaction forces, treated here as volume densities. If written for the overall structure, the resulting mechanical problem is analogous to the one derived for a one-phase continuum, where the total stress tensor is defined as the sum of the partial stresses

in the matrix and the uniaxial contributions of the reinforcements. The interesting point of such model is the possibility of considering different kinematics via the expression of the interaction forces acting in the equilibrium equations of each phase, thus allowing to account both for sliding and scale effects. The possibility of treating the different material interactions as body forces is however limited to the case where the reinforcements are continuously distributed in the matrix.

A different way of treating material heterogenities linked to embedded reinforcements is achieved by means of structural finite elements. Several authors have developed in the recent years multi-layered plate elements with high order kinematics able to reproduce complex mechanical behaviours in material stacks. Teng and Zhang [34] and Teng *et al.* [35] have developed a 4-node 24-DOFs and two 8-node 48-DOFs composite plate elements based on linear rectangular elements for modelling concrete, FRP lamina, adhesive layers and steel reinforcements. In the first case, the materials are supposed to be perfectly bonded, whereas in the second case bond-slip effects between concrete and FRP are integrated by means of an interconnecting zero-thickness finite element and through a smeared layer with finite thickness, respectively. For all the models, Timoshenko's composite beam functions are adopted for describing the transversal and rotational behaviour without occuring in shear-locking problems. A similar approach has been followed by Feldfogel and Rabinovitch [36], where a new multilayered plate element based on the Constant Strain Triangle (CST) is presented. The avantage of this model with respect to rectangular-shaped elements is the possibility to deal with irregular layouts as often happens in retrofitting applications by means of FRP. However, due to the bidimensional character of the proposed approach, this enhanced modelling is limited to a plane making it difficult to represent linear inhomogeneities devoping in the transversal direction.

Although appealing from a computational point of view, the aforementioned strategies may results to be unsuitable for modelling locally embedded linear inclusion such those employed in retrofitting operations. On one hand, the derivation of an equivalent material behaving as a Cauchy's continuum is possible, indeed, on the assumption that a sufficiently small Representative Volume Element (RVE) can be identified. On the other hand, the full three-dimensionality of the problem induced by particular inclusion topologies does not seems easily addressed by means of full 1D or 2D modelling. For these reasons, the so-called "mixed modelling" approaches have been used for bridging the gap between macroscopic and mesoscopic analysis. They consists in the combination of 3D (2D, in case of plane problems) and 1D finite element models for concrete and inclusions, respectively. In this context, Romdhane and Ulm [37] have addressed the modeling in the thermodynamics framework of two major phenomena governing the non-linear behaviour of reinforced concrete, i.e. material bond degradation and bridge effects, by means of trusses with slip degrees of freedom and interface finite elements. A similar problem has been considered by Ibrahimbegovic *et al.* [38] who have treated strain localisation in concrete and slip mechanisms at the steel-concrete interface by means of the Embedded Finite Element Method (E-FEM) [39, 24, 25, 40] and the Extended

Finite Element Method (X-FEM) [41, 42, 43, 44], respectively. Applications of the previous approach have recently been extended by Rukavina *et al.* [45] to the case of fibre-reinforced concrete. A different strategy has been followed by Casanova *et al.* [47] for modeling reinforced concrete structures by encapsulating non-coincident trusses in 8-node brick elements through a local bond stress-slip law governing the evolution of the interaction forces exchanged at the interface. In the same framework of [38] and [45], a model based on the Partition of Unity Finite Element Method (PUFEM) has been proposed by Radtke *et al.* [46], allowing the discrete treatment of several embedded fibres.

Mixed-modelling may however lead to large errors in the solution close to the inclusion zone when perfect bonding and refined meshes are adopted in the analysis. In such circumstances, being the physical cross sectional dimension of the reinforcement not taken into account by the 1D representation of the inclusion, the resulting geometrical singularity can lead to spurious stress concentrations in the matrix as pointed out by Llau *et al.* [48] and Vincent *et al.* [49]. This drawback can therefore represent a serious limitation when material nonlinearities are included in the model since non-physical material degradations can take place. For these reasons, in order to recover the physical solution at the interface, in [48] a three-dimensional volume of the inclusion is superposed to the uni-dimensional one. The weak equilibrium between the interaction force distribution computed along the axis and the 3D stress distribution inside the volume is then enforced. By doing so, the interaction forces are locally treated as an averaged volume density, as proposed in the framework of multiphase models [31, 8, 32, 33]. To the same goal, in the framework of the limit analysis of non-standard three-dimensional reinforcement layouts, in [49] the volume containing the heterogeneous material is locally replaced by an homogenised one obeying to a macroscopic strength condition. The problems raised by the 1D modelling are therefore avoided and fewer difficulties are encountered in the meshing process. The unwanted behaviours related to mixed-modelling simulations could be also mitigated by introducing a slip between the materials as the characteristic transversal mesh size tends to the characteristic dimension of the inclusion cross section. In multiscale terms, this would allow to account for scale effects associated with the transition from the macroscopic space variable to the microscopic one [31].

In the present contribution, the matrix-inclusion problem is treated from a mixed-modelling point of view. An implicit interface description is achieved for the case of linear reinforcements by means of an enriched finite element formulation obtained from the Hu-Washizu functional. The Cauchy's equilibrium equations are firstly written in terms of the microscopic space variable. The corresponding equations are then derived at the macroscale through an upscaling procedure. By assuming that the inclusion works only in traction-compression, the interaction forces exchanged between the two phases appear as localised volume density distributions defined along the reinforcement axis. In order to deal with such inhomogeneity, an additive decomposition of the displacement field into a long distance regular contribution and a term associated to the interface kinematics is introduced. It is shown that, by computing the compatible strain field, the interface force governing the

equilibrium of the reinforcement at the macroscale can be related to the discontinuity appearing in the cartesian Cauchy stress field of the matrix. This result is operated for embedding the local interface behaviour in the macroscale response of the matrix, thus allowing an easier treatment of matrix-inclusion problems. For the sake of simplicity, the developements herein are presented in the framework of linear elasticity and perfect bond between the materials but can be extended to non-linear behaviours.

The article is organised as follows. In Section 2 the governing equations of the boundary value problem are derived for the case of a linear inclusion embedded into an homogeneous isotropic matrix, for which a decomposition of the displacement field is introduced. The weak formulation and the finite element approximation are then obtained. The numerical implementation is detailed in Section 3 for plane structural problems. Computational aspects are discussed in Section 4, where the assembly and integration procedures are detailed. In Section 5 elementary and structural case studies of pull-out configurations are simulated. The proposed formulation is here compared to traditional modelling strategies both in terms of local/global responses and convergence properties of the finite element approximation. Section 6 concludes with some remarks and perspectives.

2 Governing equations

2.1 Scale description

A bounded body $\Omega \in \mathbb{R}^3$ with characteristic length L is crossed by an inclusion $\mathcal{I} \in \mathbb{R}^3$ such that $\mathcal{I} \subset \Omega$. The latter is characterised by a constant cross section A_I, axis Γ and characteristic lengths ℓ and D in the longitudinal and transverse direction, respectively (see figure 1). Introducing the physical space variable $\mathbf{X}$ of the medium and assuming $D \ll \ell$ and $\ell \sim L$, we define the dimensionless microscopic and macroscopic space variables $\mathbf{z} = \mathbf{X}/D$ and $\mathbf{x} = \mathbf{X}/L$. Due to these assumptions, at the macroscale we will consider that two opposite points belonging to the interface lie on Γ, i.e. $\mathbf{x}_\Gamma^\pm \approx \mathbf{x}_\Gamma$. By means of such two-scale scale decomposition, a generic physical quantity $e(\mathbf{X})$ can be expressed, for instance, in the form $e(\mathbf{x}, \mathbf{z})$ as:

$$e(\mathbf{X}) = e(\mathbf{x}) + \Delta e(\mathbf{z}) \tag{1}$$

where Δe is a fluctuation computed at the microscale. For an exhaustive treatment of multiscale problems, the reader is referred to [50].

2.2 Boundary value problem

Let us consider the case of linear homogeneous isotropic materials. By denoting with $\mathbb{C}_0$ and $\mathbb{C}_I$ the fourth-order elasticity tensors of the matrix and the inclusion, respectively, the Cauchy stress tensor of the latter can be expressed at the microscale as:

$$\boldsymbol{\sigma}_I(\mathbf{z}) = \mathbb{C}_0 : \boldsymbol{\varepsilon}(\mathbf{z}) + \boldsymbol{\tau}(\mathbf{z}) \tag{2}$$

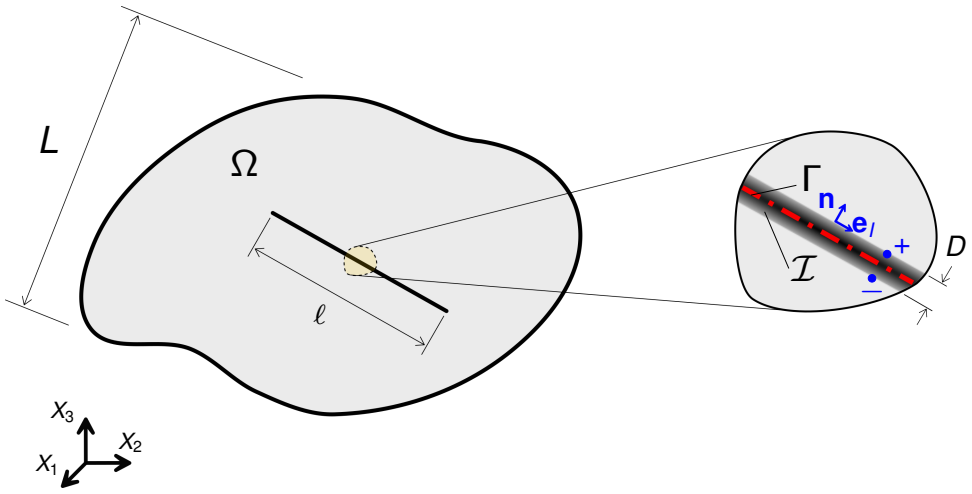

Figure 1: Matrix-inclusion problem.

where $\boldsymbol{\varepsilon} = \nabla^{s}\mathbf{u}$, with $\mathbf{u}$ the displacement field, and $\boldsymbol{\tau} = (\mathbb{C}_I - \mathbb{C}_0) : \boldsymbol{\varepsilon}$. The Cauchy's equilibrium equations can then be written as:

$$\mathbf{div}\left(\mathbb{C}_0 : \boldsymbol{\varepsilon}\left(\mathbf{z}\right)\right) + \mathbf{div}\left(\boldsymbol{\tau}\left(\mathbf{z}\right)\chi_I\left(\mathbf{z}\right)\right) = \mathbf{0}, \quad \forall \mathbf{z} \in \Omega \tag{3}$$

with χ_I the characteristic function of $\mathcal{I}$. If we develop the second term, we obtain:

$$\mathbf{div}\left(\mathbb{C}_0 : \boldsymbol{\varepsilon}\left(\mathbf{z}\right)\right) + \mathbf{div}\left(\boldsymbol{\tau}\left(\mathbf{z}\right)\right)\chi_I\left(\mathbf{z}\right) - \boldsymbol{\tau}\left(\mathbf{z}\right)\cdot\mathbf{n}\left(\mathbf{z}\right)\delta_{\partial I}\left(\mathbf{z}\right) = \mathbf{0}, \quad \forall \mathbf{z} \in \Omega \tag{4}$$

where $\mathbf{n}$ denotes the outward normal to $\mathcal{I}$ (see figure 1) and $\delta_{\partial I}$ is the Dirac delta centred on the inclusion boundary $\partial\mathcal{I}$. Furthermore, the stress vector must be continuous at every discontinuity surface, i.e.:

$$\mathbf{n}\left(\mathbf{z}\right)\cdot\left[\!\left[\boldsymbol{\sigma}\left(\mathbf{z}\right)\right]\!\right] = \mathbf{n}\left(\mathbf{z}\right)\cdot\left(\boldsymbol{\sigma}_0\left(\mathbf{z}\right) - \boldsymbol{\sigma}_I\left(\mathbf{z}\right)\right) = -\mathbf{n}\left(\mathbf{z}\right)\cdot\boldsymbol{\tau}\left(\mathbf{z}\right) = \mathbf{0}, \quad \forall \mathbf{z} \in \partial\mathcal{I} \tag{5}$$

If we take into account equation (5) and the symmetry of the stress tensor, equation (4) therefore becomes:

$$\mathbf{div}\left(\mathbb{C}_0 : \boldsymbol{\varepsilon}\left(\mathbf{z}\right)\right) + \mathbf{div}\left(\boldsymbol{\tau}\left(\mathbf{z}\right)\right)\chi_I\left(\mathbf{z}\right) = \mathbf{0}, \quad \forall \mathbf{z} \in \Omega \tag{6}$$

In order to write the macroscopic equilibrium, let us first consider the following integral of $(\bullet)$:

$$\int_\Omega (\bullet)\,\chi_I\left(\mathbf{z}\right)\,\mathrm{d}V = \int_I (\bullet)\,\mathrm{d}V_I = \int_\Gamma \langle\bullet\rangle_{A_I}\,\mathrm{d}s\,A_I = \int_\Omega \langle\bullet\rangle_{A_I}\,\delta_\Gamma\left(A_I^{-1}\mathbf{x}\right)\,\mathrm{d}V \tag{7}$$

where $\langle\bullet\rangle_{A_I}$ is the cross-sectional average of $(\bullet)$, δ_Γ is the line Dirac delta function centred on Γ and $\lambda = A_I^{-1}$ plays the role of a scale factor. Therefore, if we introduce the interaction forces $\mathbf{f}_\Gamma$ exchanged at the interface, we can write the equilibrium at the macroscale as:

$$\mathbf{div}\left(\mathbb{C}_0 : \boldsymbol{\varepsilon}\left(\mathbf{x}\right)\right) + \mathbf{f}_\Gamma\left(\mathbf{x}\right)\delta_\Gamma\left(\lambda\mathbf{x}\right) = \mathbf{0}, \quad \forall \mathbf{x} \in \Omega \tag{8}$$

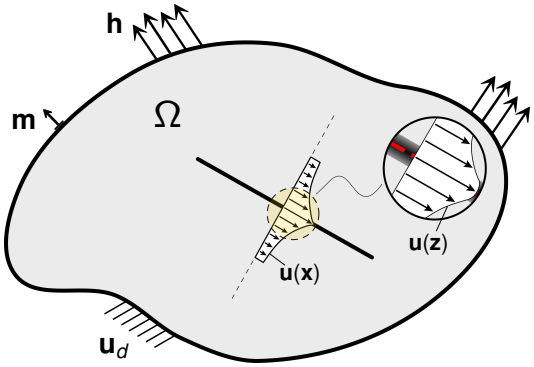

Figure 2: Boundary conditions and displacement field at the different scales of observation.

where the term $\mathbf{f}_\Gamma \, \delta_\Gamma$ must be interpreted in the sense of distributions, with $\mathbf{f}_\Gamma$ corresponding to a force density. Such quantity ensures the equilibrium of the inclusion, i.e. in case of an uniaxial behaviour:

$$\mathbf{div}\left(\sigma_I\left(\mathbf{x}\right)\mathbf{e}_I \otimes \mathbf{e}_I\right) - \mathbf{f}_\Gamma\left(\mathbf{x}\right) = \mathbf{0}, \quad \forall \mathbf{x} \in \mathcal{I} \tag{9}$$

with σ_I the uniaxial stress of the inclusion in the longitudinal direction $\mathbf{e}_I$ (see figure 1). By substituting Equation (9) into Equation (8), we end up with:

$$\mathbf{div}\left(\mathbb{C}_0 : \boldsymbol{\varepsilon}\left(\mathbf{x}\right)\right) + \mathbf{div}\left(\sigma_I\left(\mathbf{x}\right)\mathbf{e}_I \otimes \mathbf{e}_I\right)\delta_\Gamma\left(\lambda\mathbf{x}\right) = \mathbf{0}, \quad \forall \mathbf{x} \in \Omega \tag{10}$$

or in a more compact form:

$$\mathbf{div}\left(\mathbb{C}_0 : \boldsymbol{\varepsilon}\left(\mathbf{x}\right)\right) + \mathbf{f}_I\left(\mathbf{x}\right)\delta_\Gamma\left(\lambda\mathbf{x}\right) = \mathbf{0}, \quad \forall \mathbf{x} \in \Omega \tag{11}$$

with

$$\mathbf{f}_I\left(\mathbf{x}\right) = \mathbf{div}\left(\sigma_I\left(\mathbf{x}\right)\mathbf{e}_I \otimes \mathbf{e}_I\right) \tag{12}$$

Equation (10) is then completed with Dirichlet and Neumann boundary conditions applied on the respective portions of the boundary $\partial\Omega = \partial_u\Omega \cup \partial_t\Omega$ such that $\partial_u\Omega \cap \partial_t\Omega = \emptyset$:

$$\begin{cases} \mathbf{u}\left(\mathbf{x}\right) = \mathbf{u}_d\left(\mathbf{x}\right) & \forall \mathbf{x} \in \partial_u\Omega \quad (13a) \\ \mathbf{m}\left(\mathbf{x}\right) \cdot \boldsymbol{\sigma}\left(\mathbf{x}\right) = \mathbf{h}\left(\mathbf{x}\right) & \forall \mathbf{x} \in \partial_t\Omega \quad (13b) \end{cases}$$

where $\mathbf{m}$ is the outward normal to $\partial\Omega$ as depicted in figure 2.

2.3 Kinematics

The problem formulated at the macroscale in section 2.2 corresponds to the case of an elastic rod embedded into a matrix whose solution presents a logarithmic singularity at the inclusion ends [1, 3]. For such reason, we express the displacement field solution of equation (8) as the sum of two contributions:

$$\mathbf{u}\left(\mathbf{x}\right) = \bar{\mathbf{u}}\left(\mathbf{x}\right) + \hat{\mathbf{u}}\left(\mathbf{x}\right), \quad \forall \mathbf{x} \in \Omega \tag{14}$$

where $\bar{\mathbf{u}}$ denotes a long distance regular contribution compatible with the strain field $\bar{\boldsymbol{\varepsilon}} = \nabla^{\mathrm{s}}\bar{\mathbf{u}}$ and satisfying the homogeneous equation:

$$\mathbf{div}\left(\bar{\boldsymbol{\sigma}}\left(\mathbf{x}\right)\right) = \mathbf{div}\left(\mathbb{C}_0 : \bar{\boldsymbol{\varepsilon}}\left(\mathbf{x}\right)\right) = \mathbf{0}, \quad \forall \mathbf{x} \in \Omega \tag{15}$$

with modified boundary conditions:

$$\begin{cases} \bar{\mathbf{u}}\left(\mathbf{x}\right) = \mathbf{u}_d\left(\mathbf{x}\right) - \hat{\mathbf{u}}\left(\mathbf{x}\right) & \forall \mathbf{x} \in \partial_u\Omega \quad (16a) \\ \mathbf{n}\cdot\bar{\boldsymbol{\sigma}}\left(\mathbf{x}\right) = \mathbf{h}\left(\mathbf{x}\right) - \mathbf{n}\cdot\hat{\boldsymbol{\sigma}}\left(\mathbf{x}\right) & \forall \mathbf{x} \in \partial_t\Omega \quad (16b) \end{cases}$$

and $\hat{\mathbf{u}}$ the solution of equation (8). The strains $\hat{\boldsymbol{\varepsilon}} = \nabla^{\mathrm{s}}\hat{\mathbf{u}}$ and the stresses $\hat{\boldsymbol{\sigma}}$ are then derived from the displacement field $\hat{\mathbf{u}}$. For what concerns the microscopic displacement field, we will assume that it is characterised by a fluctuation $\Delta\mathbf{u}(\mathbf{z})$ about its interface value $\mathbf{u}_\Gamma^\pm$ and that the latter can be related to the macroscopic displacement by setting $\mathbf{u}_\Gamma^\pm\left(\mathbf{z}\right) \approx \mathbf{u}_\Gamma\left(\mathbf{x}\right)$. Such hypothesis allows us to state the equivalence between the microscopic and macroscopic interface strain fields, i.e. $\boldsymbol{\varepsilon}_\Gamma^\pm\left(\mathbf{z}\right) \approx \boldsymbol{\varepsilon}_\Gamma^\pm\left(\mathbf{x}\right)$.

2.4 Interface behaviour

At the interface, due to the uniaxial behaviour of the inclusion (see figure 3), the displacement can be expressed in terms of its longitudinal component $\hat{u}_s^\Gamma$ as:

$$\hat{\mathbf{u}}_\Gamma\left(\mathbf{x}\right) = \hat{u}_s^\Gamma\left(\mathbf{x}\right)\mathbf{e}_I, \quad \forall \mathbf{x} \in \Gamma \tag{17}$$

On two opposite sides of the interface, the compatible strain reads:

$$\boldsymbol{\varepsilon}_\Gamma^-\left(\mathbf{x}\right) = \nabla^{\mathrm{s}}\bar{\mathbf{u}}|_\Gamma + \nabla^{\mathrm{s}}\hat{\mathbf{u}}_\Gamma^- \qquad \boldsymbol{\varepsilon}_\Gamma^+\left(\mathbf{x}\right) = \nabla^{\mathrm{s}}\bar{\mathbf{u}}|_\Gamma + \nabla^{\mathrm{s}}\hat{\mathbf{u}}_\Gamma^+ \tag{18}$$

where $\nabla^{\mathrm{s}}\hat{\mathbf{u}}_\Gamma^- = (\hat{u}_{s,\xi}^{\Gamma-}\mathbf{n}\otimes\mathbf{e}_I)^{\mathrm{s}}$ and $\nabla^s\hat{\mathbf{u}}_\Gamma^+ = (\hat{u}_{s,\xi}^{\Gamma+}\mathbf{n}\otimes\mathbf{e}_I)^{\mathrm{s}}$ with $\hat{u}_{s,\xi}^{\Gamma-} > 0$ and $\hat{u}_{s,\xi}^{\Gamma+} < 0$, as can be checked in figure 3b. Indicial notation has here been adopted, with subscripts preceded by commas denoting partial derivatives with respect to the local spatial coordinates s and ξ. In particular, we will assume that $\hat{u}_s^\Gamma$ is homogeneous in s, i.e. $\hat{u}_{s,s}^\Gamma = 0$, which corresponds to the case of a rigid inclusion [1]. Moreover, the interface force $\mathbf{f}_\Gamma$ defined at the macroscale can be computed by requiring that the virtual work done by the density field $\mathbf{f}_\Gamma\,\delta_\Gamma$ is equal to the work done by the microscopic boundary tractions $\mathbf{t}_{\partial I}$ acting on the concrete phase:

$$\int_\Omega \mathbf{f}_\Gamma(\mathbf{x})\,\delta_\Gamma(\lambda\mathbf{x})\cdot\mathbf{u}_v(\mathbf{x})\,\mathrm{d}V = \int_{\partial\mathcal{I}} \mathbf{t}_{\partial I}(\mathbf{z})\cdot\mathbf{u}_v(\mathbf{z})\,\mathrm{d}S \quad , \quad \forall\,\mathbf{u}_v(\mathbf{z})\,,\mathbf{u}_v(\mathbf{x}) \in \mathcal{U}_0 \tag{19}$$

with $\mathbf{u}_v(\mathbf{z})$ and $\mathbf{u}_v(\mathbf{x})$ belonging to the set of kinematically admissible displacements $\mathcal{U}_0$ (see next section). After few developments, by considering a cylindrical inclusion of radius $r = D/2$ and denoting with $\mathbf{t}_\Gamma^- = \mathbf{t}_{\partial I}(\theta) = \mathbf{n}(\theta)\cdot\boldsymbol{\sigma}_0(\theta)$ and $\mathbf{t}_\Gamma^+ = \mathbf{t}_{\partial I}(\theta+\pi) = -\mathbf{n}(\theta)\cdot\boldsymbol{\sigma}_0(\theta+\pi)$ (sign convention in figure 3b for a 2D section), the previous equation becomes:

$$\lambda^{-1}\int_\Gamma \mathbf{f}_\Gamma(\mathbf{x})\,\cdot\,\mathbf{u}_{\Gamma v}(\mathbf{x})\,\mathrm{d}s = \int_\Gamma\int_0^\pi \left(\mathbf{t}_\Gamma^- + \mathbf{t}_\Gamma^+\right)\,r\,d\theta\cdot\mathbf{u}_{\Gamma v}(\mathbf{x})\,\mathrm{d}s \quad , \quad \forall\,\mathbf{u}_{\Gamma v}(\mathbf{x}) \tag{20}$$

[1] Such hypothesis appears reasonable if the stiffness contrast between the matrix and the inclusion is high, as usually happens, for instance, in structures involving anchoring systems.

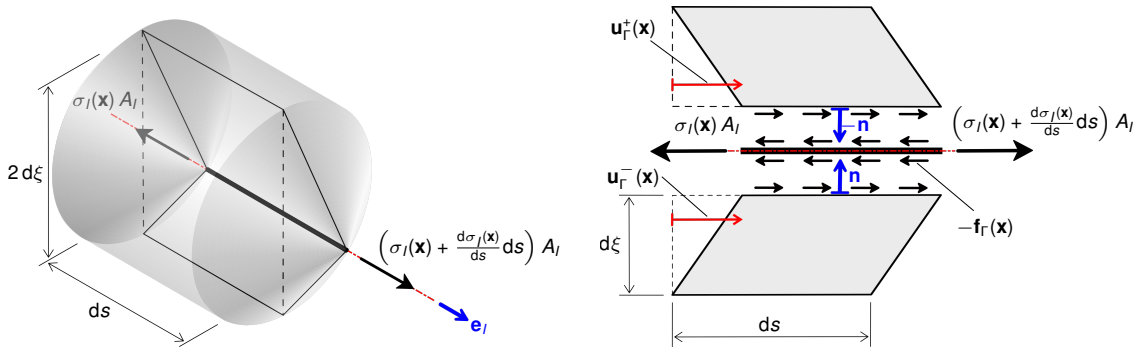

(a) (b)

Figure 3: Local behaviour of an elastic rod embedded in an isotropic matrix. Three-dimensional (a) and two-dimensional (b) representations.

where the hypothesis $\mathbf{u}_\Gamma^\pm(\mathbf{z}) \approx \mathbf{u}_\Gamma(\mathbf{x})$ made in section 2.3 has been taken into account. By deriving with respect to s and collecting the terms, one obtains:

$$\left(\lambda^{-1}\mathbf{f}_\Gamma(\mathbf{x}) - \int_0^\pi \left(\mathbf{n}\cdot\boldsymbol{\sigma}_0^- - \mathbf{n}\cdot\boldsymbol{\sigma}_0^+\right) r\,\mathrm{d}\theta\right)\cdot\mathbf{u}_{\Gamma v}(\mathbf{x}) = 0 \quad , \quad \forall\,\mathbf{u}_{\Gamma v}(\mathbf{x}) \tag{21}$$

By recalling that $\boldsymbol{\sigma}_0^\pm(\mathbf{z}) \approx \mathbb{C}_0 : \boldsymbol{\varepsilon}_\Gamma^\pm(\mathbf{x})$ (see section 2.3) and due to the arbitrariness of $\mathbf{u}_{\Gamma v}(\mathbf{x})$, we end up with:

$$\begin{aligned}
\mathbf{f}_\Gamma(\mathbf{x}) &= \int_0^\pi \left(\mathbf{n}\cdot\left(\mathbb{C}_0 : \nabla^{\mathrm{s}}\hat{\mathbf{u}}_\Gamma^-\right) - \mathbf{n}\cdot\left(\mathbb{C}_0 : \nabla^{\mathrm{s}}\hat{\mathbf{u}}_\Gamma^+\right)\right) r\,\mathrm{d}\theta\,\lambda \\
&= \int_0^\pi \left(\mathbf{n}\cdot\left[\mathbb{C}_0 : \hat{u}_{s,\xi}^{\Gamma-}\left(\mathbf{n}\otimes\mathbf{e}_I\right)^{\mathrm{s}}\right] - \mathbf{n}\cdot\left[\mathbb{C}_0 : \hat{u}_{s,\xi}^{\Gamma+}\left(\mathbf{n}\otimes\mathbf{e}_I\right)^{\mathrm{s}}\right]\right) r\,\mathrm{d}\theta\lambda \\
&= -\int_0^\pi [\![\hat{\tau}]\!] r\,\mathrm{d}\theta\,\mathbf{e}_I\,\lambda = \frac{2}{r}\tau_\Gamma\mathbf{e}_I
\end{aligned} \tag{22}$$

where $[\![\hat{\tau}]\!] = \hat{\tau}_\Gamma^+ - \hat{\tau}_\Gamma^- = \mathbf{n}\cdot\hat{\boldsymbol{\sigma}}_\Gamma^+\cdot\mathbf{e}_I - \mathbf{n}\cdot\hat{\boldsymbol{\sigma}}_\Gamma^-\cdot\mathbf{e}_I$ denotes the shear stress jump between two opposite sides of the interface and

$$\tau_\Gamma = -\frac{1}{2\pi}\int_0^\pi [\![\hat{\tau}]\!]\,\mathrm{d}\theta \tag{23}$$

denotes the average interface shear stress computed over the boundary. As expected, it is shown that the stress $\bar{\boldsymbol{\sigma}}$ associated with the long distance contribution $\bar{\mathbf{u}}$ does not participate in the computation of $\mathbf{f}_\Gamma$ responsible for the equilibrium of the inclusion at the macroscale.

2.5 Weak formulation and finite element framework

We will start from the mixed Hu-Washizu variational principle applied to equation (11) by defining the three solution spaces for displacements $\mathcal{U} = \{\mathbf{u}\,|\,\mathbf{u} \in H^1(\Omega),\ \mathbf{u} = \mathbf{u}_d \text{ on } \partial_{\mathrm{u}}\Omega\}$, strains $\mathcal{E} = \{\boldsymbol{\varepsilon}\,|\,\boldsymbol{\varepsilon} \in L^2(\Omega)\}$ and stresses $\mathcal{S} = \{\boldsymbol{\sigma}\,|\,\boldsymbol{\sigma} \in$

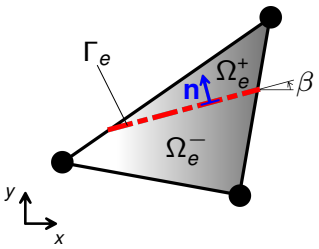

Figure 4: Decomposition of a CST element crossed by a linear inclusion.

$L^2(\Omega)\}$. Therefore, for all arbitrary virtual field $\mathbf{u}_v \in \mathcal{U}_0 = \{\mathbf{u} \,|\, \mathbf{u} \in H^1(\Omega),\, \mathbf{u} = \mathbf{0} \text{ on } \partial_u\Omega\}$, $\boldsymbol{\tau} \in \mathcal{S}$ and $\boldsymbol{\gamma} \in \mathcal{E}$, the following system of equations is derived:

$$\begin{cases} \displaystyle\int_\Omega \boldsymbol{\sigma} : \nabla^s \mathbf{u}_v \, \mathrm{d}V - A_I \int_\Gamma \mathbf{f}_I \cdot \mathbf{u}_v \, \mathrm{d}s - \int_{\partial_t\Omega} \mathbf{h} \cdot \mathbf{u}_v \, \mathrm{d}S = 0 & \text{(24a)} \\ \displaystyle\int_\Omega \boldsymbol{\tau} \cdot (\nabla^s \mathbf{u} - \boldsymbol{\varepsilon}) \, \mathrm{d}V = 0 & \text{(24b)} \\ \displaystyle\int_\Omega \boldsymbol{\gamma} \cdot (\mathbb{C}_0 : \boldsymbol{\varepsilon} - \boldsymbol{\sigma}) \, \mathrm{d}V = 0 & \text{(24c)} \end{cases}$$

with forces $\mathbf{f}_I$ acting as external loads. We then introduce the Finite Element discretisations Ω_h and Γ_h of Ω and Γ, respectively, where the elementary segments $\Gamma_e \subset \Gamma_h$ are defined by the intersections of Γ with the subsets $\Omega_e \subset \Omega_h$. By means of the matrix notation, we then introduce the following kinematic approximations for Ω_h:

$$\mathbf{u} \approx \mathbf{u}_h = \mathbf{N}\mathbf{d} + \mathbf{N}_\alpha \boldsymbol{\alpha} \qquad\qquad \boldsymbol{\varepsilon} \approx \boldsymbol{\varepsilon}_h = \mathbf{B}\mathbf{d} + \mathbf{B}_\zeta \boldsymbol{\zeta} \tag{25}$$

where $\mathbf{d}$ are the nodal displacements and $\boldsymbol{\alpha}$ and $\boldsymbol{\zeta}$ are kinematic enhancements defined at the element level. Furthermore, $\mathbf{N}$ and $\mathbf{N}_\alpha$ denote the displacement interpolation matrices, whereas $\mathbf{B} = \mathbf{L}\mathbf{N}$ and $\mathbf{B}_\zeta$ are the strain interpolation matrices, with $\mathbf{L}$ computing ∇^s. We make then the hypothesis that $\mathbf{u}_h$ is compatible with the strains $\boldsymbol{\varepsilon}_h$, which requires $\boldsymbol{\alpha} \equiv \boldsymbol{\zeta}$ and $\mathbf{B}_\zeta = \mathbf{B}_\alpha = \mathbf{L}\mathbf{N}_\alpha$. In addition, we will assume that the computed stresses satisfy the constitutive law, i.e. $\boldsymbol{\sigma}_h = \mathbf{D}\boldsymbol{\varepsilon}_h$, with $\mathbf{D}$ denoting the stiffness matrix of the material. Due to these assumptions, equations (24b) and (24c) are identically satisfied. For what concerns the virtual fields, we make then the following choice:

$$\mathbf{u}_v \approx \mathbf{u}_{vh} = \mathbf{N}\mathbf{d}_v + \mathbf{N}^*_\alpha \boldsymbol{\alpha}_v \qquad\qquad \boldsymbol{\varepsilon}_v \approx \boldsymbol{\varepsilon}_{vh} = \mathbf{B}\mathbf{d}_v + \mathbf{B}^*_\zeta \boldsymbol{\zeta}_v \tag{26}$$

where $\mathbf{d}_v$, $\boldsymbol{\alpha}_v$ and $\boldsymbol{\zeta}_v$ have the same meaning as in equation (25) and $\mathbf{B}^*_\zeta$ is the interpolation matrix of the virtual strain enhancement. Also in this case, we make the hypothesis $\boldsymbol{\alpha}_v \equiv \boldsymbol{\zeta}_v$ and $\mathbf{B}^*_\zeta = \mathbf{B}^*_\alpha = \mathbf{L}\mathbf{N}^*_\alpha$. The proposed formulation therefore corresponds to a Petrov-Galerkin approach where the test functions and the solution functions belong to different spaces [51, 52]. A similar approach has been proposed in the framework of the E-FEM and it goes under the name of "Statically and Kinematically Optimal Non-symmetric" (SKON) formulation (see for instance [53]).

The result is a non-conforming finite element model whose convergence is ensured by requiring that the elementary patch test is satisfied [54, 55, 56], i.e. by imposing:

$$\int_{\Omega_e} (\mathbf{B}_\alpha^*)^\mathsf{T} \, \mathrm{d}V = \mathbf{0} \tag{27}$$

With the previous approximations, problem (24) is restated as:

$$\begin{aligned} \forall (\mathbf{d}_v, \boldsymbol{\alpha}_v), \quad & \mathbf{d}_v \left(\int_{\Omega_h} \mathbf{B}^\mathsf{T} \boldsymbol{\sigma}_h \, \mathrm{d}V - A_I \int_{\Gamma_h} \mathbf{N}^\mathsf{T} \mathbf{f}_I \, \mathrm{d}s - \int_{\partial_t \Omega_h} \mathbf{N}^\mathsf{T} \mathbf{h} \, \mathrm{d}S \right) + \\ & + \boldsymbol{\alpha}_v \left(\int_{\Omega_h} (\mathbf{B}_\alpha^*)^\mathsf{T} \boldsymbol{\sigma}_h \, \mathrm{d}V - A_I \int_{\Gamma_h} (\mathbf{N}_\alpha^*)^\mathsf{T} \mathbf{f}_I \, \mathrm{d}s - \int_{\partial_t \Omega_h} (\mathbf{N}_\alpha^*)^\mathsf{T} \mathbf{h} \, \mathrm{d}S \right) = 0 \end{aligned} \tag{28}$$

where the term $\int_{\partial_t \Omega_h} (\mathbf{N}_\alpha^*)^\mathsf{T} \mathbf{h} \, \mathrm{d}S$ may be neglected compared to the major contribution associated with $\mathbf{f}_I$ according to usual embedded formulations [53]. Such hypothesis corresponds to say that the loads are applied outside the enhanced region. Due to the arbitrariness of $\mathbf{d}_v$ and $\boldsymbol{\alpha}_v$ we end up with the following system of equations:

$$\begin{cases} \displaystyle\int_{\Omega_h} \mathbf{B}^\mathsf{T} \boldsymbol{\sigma} \, \mathrm{d}V = A_I \int_{\Gamma_h} \mathbf{N}^\mathsf{T} \mathbf{f}_I \, \mathrm{d}s + \int_{\partial_t \Omega_h} \mathbf{N}^\mathsf{T} \mathbf{h} \, \mathrm{d}S & \text{(29a)} \\ \displaystyle\int_{\Omega_h} (\mathbf{B}_\alpha^*)^\mathsf{T} \boldsymbol{\sigma} \, \mathrm{d}V = A_I \int_{\Gamma_h} (\mathbf{N}_\alpha^*)^\mathsf{T} \mathbf{f}_I \, \mathrm{d}s & \text{(29b)} \end{cases}$$

To lighten the notation, the subscripts denoting the discretized problem and the elasticity of the matrix will be dropped when no confusion is likely to arise.

3 2D implementation

In the bidimensional setting, the inclusion $\mathcal{I}$ of length ℓ and inclination β cuts at the macroscale the elementary domain Ω_e of thickness t into two subdomains Ω_e^- and Ω_e^+ identified by the unitary normal vector $\mathbf{n}$, as depicted in figure 4 for a Constant Strain Triangle (CST). We focus for the moment on the case of a single finite element, i.e. we set $\Omega \equiv \Omega_e$ and $\Gamma \equiv \Gamma_e$.

3.1 Real fields

For what concerns the real fields, we define the interpolation matrix $\mathbf{N}_\alpha = N_\alpha \mathbf{I}_2$, with $\mathbf{I}_2$ the (2×2) identity matrix and function N_α chosen such that the kinematic boundary conditions can still be expressed in terms of the sole nodal displacements, which consists in imposing $N_\alpha(\mathbf{x}_i) = 0$ for all node i. We make, then, the following choice for function N_α:

$$N_\alpha(\mathbf{x}) = \chi_- \sum_{i=1}^{N} a_i \mathcal{H}_\Gamma(\mathbf{x}_i) N_i(\mathbf{x}) + \chi_+ \sum_{i=1}^{N} a_i (1 - \mathcal{H}_\Gamma(\mathbf{x}_i)) N_i(\mathbf{x}) \tag{30}$$

where N_i is the shape function of node i, χ_- and χ_+ are the characteristic functions of Ω^- and Ω^+, respectively, and $\mathcal{H}_\Gamma(\mathbf{x}_i)$ are the values at nodes of the Heaviside

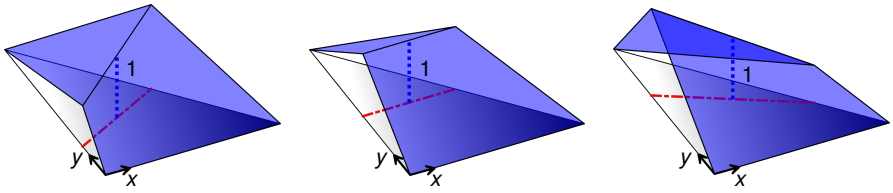

(a) (b) (c)

Figure 5: Function N_α in case of CST elements for different orientations of the inclusion: (a) $\beta = -20°$, (b) $\beta = 0°$, (c) $\beta = 20°$.

function centered on Γ. Coefficients a_i are computed requiring $N_\alpha\left(\mathbf{x}_\Gamma^G\right) = 1$ and such that a C^0- continuity is ensured along Γ, i.e.:

$$\sum_{i=1}^{N} a_i(1 - 2\mathcal{H}_\Gamma(\mathbf{x}_i))N_i = 0, \quad \text{on } \Gamma \tag{31}$$

Note that condition (31) implies that the longitudinal component $N_{\alpha,s} = \mathbf{e}_I^\mathsf{T}\nabla N_\alpha$ evaluated on Γ is continuous, i.e. $N^-_{\alpha,s}|_\Gamma = N^+_{\alpha,s}|_\Gamma$. Figure 5 shows function N_α in case of CST elements for different orientations of the inclusion. From expression (30), it therefore appears that matrix $\mathbf{N}_\alpha$ is expressed as a linear combination of the standard shape function basis $\mathbf{N}_i = N_i\mathbf{I}_2$ with $i = 1, \ldots, N$, as:

$$\mathbf{N}_\alpha = \chi_- \sum_{i=1}^{N} a_i\mathcal{H}_\Gamma(\mathbf{x}_i)\mathbf{N}_i + \chi_+ \sum_{i=1}^{N} a_i(1 - \mathcal{H}_\Gamma(\mathbf{x}_i))\mathbf{N}_i \tag{32}$$

Analogously, the strain interpolation matrix $\mathbf{B}_\alpha = \mathbf{L}\mathbf{N}_\alpha$ is computed by combining matrices $\mathbf{B}_i = \mathbf{L}\mathbf{N}_i$:

$$\begin{aligned}\mathbf{B}_\alpha &= \chi_- \sum_{i=1}^{N} a_i\mathcal{H}_\Gamma(\mathbf{x}_i)\mathbf{B}_i + \chi_+ \sum_{i=1}^{N} a_i(1 - \mathcal{H}_\Gamma(\mathbf{x}_i))\mathbf{B}_i \\ &= \chi_- \left(N^-_{\alpha,s}\,\mathbf{q} + N^-_{\alpha,\xi}\mathbf{p}\right) + \chi_+ \left(N^+_{\alpha,s}\,\mathbf{q} + N^+_{\alpha,\xi}\mathbf{p}\right)\end{aligned} \tag{33}$$

where in the last expression we used the longitudinal and normal components $N_{\alpha,s}$ and $N_{\alpha,\xi}$ of the gradient ∇N_α and adopted the matrices:

$$\mathbf{q} = \begin{bmatrix} e_{Ix} & 0 \\ 0 & e_{Iy} \\ e_{Iy} & e_{Ix} \end{bmatrix} \qquad \mathbf{p} = \begin{bmatrix} n_x & 0 \\ 0 & n_y \\ n_y & n_x \end{bmatrix} \tag{34}$$

3.2 Virtual fields

The virtual displacement interpolation matrix is computed as $\mathbf{N}^*_\alpha = N^*_\alpha\mathbf{I}_2$ with function N^*_α defined as follows:

$$N^*_\alpha(\mathbf{x}) = \chi_- \left(1 + \frac{1}{k_-}\left(\mathbf{x} - \mathbf{x}_\Gamma^G\right)^\mathsf{T}\mathbf{n}\right) + \chi_+ \left(1 - \frac{1}{k_+}\left(\mathbf{x} - \mathbf{x}_\Gamma^G\right)^\mathsf{T}\mathbf{n}\right) \tag{35}$$

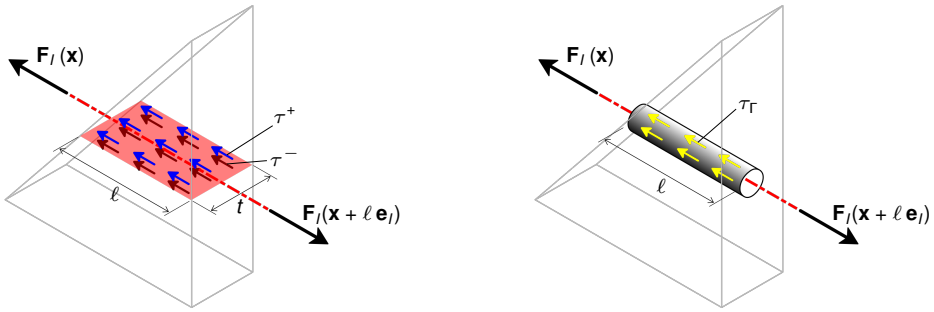

(a) (b)

Figure 6: Shear stresses on the discontinuity surface (a), interface stresses acting on the inclusion boundary (b).

where $k_- = A^-/\ell$, $k_+ = A^+/\ell$ and A^-, A^+ are the plane measures of Ω^- and Ω^+, respectively. Computing $\mathbf{L}\mathbf{N}^*_\alpha$ gives the expression of matrix $\mathbf{B}^*_\alpha$:

$$\mathbf{B}^*_\alpha = \left(\frac{1}{k_-}\chi_- - \frac{1}{k_+}\chi_+\right)\mathbf{p} \tag{36}$$

It is easy to check that such matrix verifies condition (27), since we have:

$$\begin{aligned}\int_\Omega (\mathbf{B}^*_\alpha)^\mathsf{T}\,\mathrm{d}V &= \int_{A^-}\frac{1}{k_-}\mathbf{p}^\mathsf{T}\,\mathrm{d}A\,t - \int_{A^+}\frac{1}{k_+}\mathbf{p}^\mathsf{T}\,\mathrm{d}A\,t \\ &= \ell\,\mathbf{p}^\mathsf{T} - \ell\,\mathbf{p}^\mathsf{T} = \mathbf{0}\end{aligned} \tag{37}$$

3.3 Resulting equations

3.3.1 Local equation

Substituting expression (36) into equation (29b) and evaluating matrix $\mathbf{N}^*_\alpha$ on Γ gives:

$$\ell\frac{1}{A^-}\int_{A^-}\mathbf{p}^\mathsf{T}\boldsymbol{\sigma}^-\,\mathrm{d}A\,t - \ell\frac{1}{A^+}\int_{A^+}\mathbf{p}^\mathsf{T}\boldsymbol{\sigma}^+\,\mathrm{d}A\,t = A_I\int_\Gamma \mathbf{f}_I\,\mathrm{d}s \tag{38}$$

with t denoting the finite element thickness. The previous result states the equilibrium between the resultant of the average stresses $\boldsymbol{\Sigma}^- = \frac{1}{A^-}\int_{A^-}\boldsymbol{\sigma}^-\,\mathrm{d}A$ and $\boldsymbol{\Sigma}^{(e),+} = \frac{1}{A^+}\int_{A^+}\boldsymbol{\sigma}^+\,\mathrm{d}A$ acting on the discontinuity surface identified by the normal $\mathbf{n}$ and the increment of the axial force of the inclusion $\Delta\mathbf{F}_I = A_I\int_\Gamma \mathbf{f}_I\,\mathrm{d}s$ and it can be rewritten in terms of the average stress jump $[\![\boldsymbol{\Sigma}]\!] = \boldsymbol{\Sigma}^+ - \boldsymbol{\Sigma}^-$ as:

$$-\ell\,\mathbf{p}^\mathsf{T}[\![\boldsymbol{\Sigma}]\!]\,t = \Delta\mathbf{F}_I \tag{39}$$

Enforcing the equilibrium of the inclusion under the average interface shear stress distribution, i.e. $\Delta\mathbf{F}_I = \tau_\Gamma S_{lat}\mathbf{e}_I$, allows us to express τ_Γ in terms of the stress field in the bulk:

$$\tau_\Gamma = -\mathbf{e}_I^\mathsf{T}\mathbf{p}^\mathsf{T}\frac{[\![\boldsymbol{\Sigma}]\!]}{S_{lat}}\ell\,t \tag{40}$$

where S_{lat} is the lateral surface of the inclusion. A representation of the local stresses developing in the bulk and at the interface is given in figure 6.

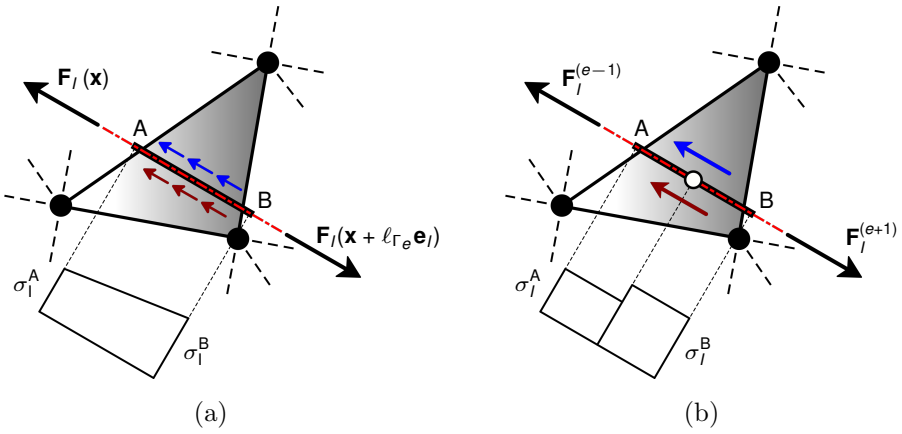

(a) (b)

Figure 7: Local (a) and global (b) problems.

3.3.2 Global equation

Being the interface stress τ_Γ defined by relation (40) constant along Γ, we replace $\mathbf{f}_I = \frac{\mathrm{d}\sigma_I(\mathbf{x})}{\mathrm{d}s}\mathbf{e}_I$ by its average value [2], i.e. $\mathbf{f}_I = \Delta\mathbf{F}_I/(A_I\ell)$. Such hypothesis would be equivalent to choose a linear interpolation of the inclusion stress and enforcing the verification of the static boundary conditions applied at its ends. Replacing the expression of $\mathbf{f}_I$ into equation (29a) gives:

$$\int_A \mathbf{B}^\mathsf{T}\boldsymbol{\sigma}\,\mathrm{d}A\,t = \frac{\int_\Gamma \mathbf{N}^\mathsf{T}\,\mathrm{d}s}{\ell}\,\Delta\mathbf{F}_I + \int_{\Gamma_t}\mathbf{N}^\mathsf{T}\mathbf{h}\,\mathrm{d}s\,t \tag{41}$$

We focus now upon the first term of the right-hand side of equation (41). Recalling that the position of the center of gravity of segment Γ can be computed for iso-parametric finite elements both as $\mathbf{x}^G = \frac{1}{\ell}\int_\Gamma \mathbf{N}\,\mathrm{d}\Gamma\mathbf{x}_N$ and $\mathbf{x}^G = \mathbf{N}^G\mathbf{x}_N$, with $\mathbf{x}_N$ the vector of nodal coordinates, allows us to write:

$$\left(\frac{\int_\Gamma \mathbf{N}\,\mathrm{d}\Gamma}{\ell} - \mathbf{N}^G\right)\mathbf{x}_N = \mathbf{0} \tag{42}$$

Let us now consider the two systems of nodal forces:

$$\mathbf{F}_1 = \frac{\int_\Gamma \mathbf{N}^\mathsf{T}\,\mathrm{d}\Gamma}{\ell}\Delta\mathbf{F}_I \tag{43}$$

$$\mathbf{F}_2 = \left(\mathbf{N}^G\right)^\mathsf{T}\Delta\mathbf{F}_I \tag{44}$$

Thanks to the partition-of-unity property of the finite element shape functions, such systems have the same resultant equal to $\Delta\mathbf{F}_I$ and if we compute the difference between the moments generated by the two systems with respect to an arbitrary point O we obtain:

$$\begin{aligned}\mathbf{M}_O^1 - \mathbf{M}_O^2 &= \sum_{i=1}^{N}\left(\frac{\int_\Gamma N_i\,\mathrm{d}\Gamma}{\ell} - N_i^G\right)\Delta\mathbf{F}_I\,(\mathbf{x}_i - \mathbf{x}_O)\\ &= \Delta\mathbf{F}_I\left(\frac{\int_\Gamma \mathbf{N}\,\mathrm{d}\Gamma}{\ell} - \mathbf{N}^G\right)\mathbf{x}_N\end{aligned} \tag{45}$$

[2] This is an arbitrary choice that can be eventually removed.

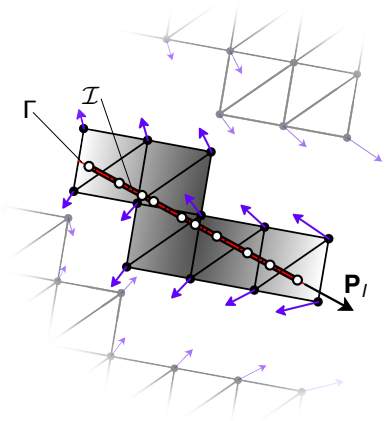

Figure 8: Global modeling.

which vanishes due to equation (42). We can therefore verify that systems $\mathbf{F}_1$ and $\mathbf{F}_2$ are statically equivalent and for such reason we restate the global equilibrium equation (41) as:

$$\int_A \mathbf{B}^\mathsf{T}\boldsymbol{\sigma}\,\mathrm{d}A\,t = (\mathbf{N}^G)^\mathsf{T}\,\Delta\mathbf{F}_I + \int_{\Gamma_t} \mathbf{N}^\mathsf{T}\mathbf{h}\,\mathrm{d}s\,t \tag{46}$$

Thus the effect of an embedded inclusion can be modeled at the global level through a force applied in the center of gravity of the segment Γ. In order to achieve such representation, truss elements can be adopted in the finite element model, as schematised in figures 7 and 8.

4 Numerical aspects

After introducing the material stiffness matrix $\mathbf{D}$ for plane linear elasticity, the overall system of equations can be derived by substituting the expression of the stress associated with the strain approximation (25):

$$\boldsymbol{\sigma} = \mathbf{DBd} + \mathbf{DB}_\alpha\boldsymbol{\alpha} \tag{47}$$

into equations (41) and (38):

$$\begin{cases} \mathbf{K}^e_{dd}\mathbf{d}_e + \mathbf{K}^e_{d\alpha}\boldsymbol{\alpha}_e = (\mathbf{N}^G_e)^\mathsf{T}\,\Delta\mathbf{F}^e_I + \mathbf{F}^e_{ext} & \text{(48a)} \\ \mathbf{K}^e_{\alpha d}\mathbf{d}_e + \mathbf{K}^e_{\alpha\alpha}\boldsymbol{\alpha}_e = \Delta\mathbf{F}^e_I & \text{(48b)} \end{cases}$$

where we have set

$$\mathbf{K}^e_{dd} = \int_{\Omega_e} \mathbf{B}^\mathsf{T}\mathbf{D}\mathbf{B}\,\mathrm{d}V \tag{49}$$

$$\mathbf{K}^e_{d\alpha} = \int_{\Omega_e} \mathbf{B}^\mathsf{T}\mathbf{D}\mathbf{B}_\alpha\,\mathrm{d}V \tag{50}$$

$$\mathbf{K}^e_{\alpha d} = \int_{\Omega_e} (\mathbf{B}^*_\alpha)^\mathsf{T}\,\mathbf{D}\mathbf{B}\,\mathrm{d}V \tag{51}$$

$$\mathbf{K}^e_{\alpha\alpha} = \int_{\Omega_e} (\mathbf{B}^*_\alpha)^\mathsf{T}\,\mathbf{D}\mathbf{B}_\alpha\,\mathrm{d}V \tag{52}$$

$$\mathbf{F}^e_{ext} = \int_{\partial_t\Omega_e} \mathbf{N}^\mathsf{T}\mathbf{h}\,\mathrm{d}S \tag{53}$$

The force increment $\Delta\mathbf{F}^e_I = \mathbf{F}^{e+1}_I - \mathbf{F}^{e-1}_I$ is computed between adjacent elements in case of perfect bond by writing a kinematic relation between the displacement of the two phases computed at the center of gravity of the inclusion, resulting into the following expression of the axial forces:

$$\begin{cases} \mathbf{F}^{e-1}_I = k_{(e,e-1)}\mathbf{T}\left[\left(\mathbf{N}^G_e\mathbf{d}_e + \boldsymbol{\alpha}_e\right) - \left(\mathbf{N}^G_{e-1}\mathbf{d}_{e-1} + \boldsymbol{\alpha}_{e-1}\right)\right] & \text{(54a)} \\ \mathbf{F}^{e+1}_I = k_{(e,e+1)}\mathbf{T}\left[\left(\mathbf{N}^G_{e+1}\mathbf{d}_{e+1} + \boldsymbol{\alpha}_{e+1}\right) - \left(\mathbf{N}^G_e\mathbf{d}_e + \boldsymbol{\alpha}_e\right)\right] & \text{(54b)} \end{cases}$$

with $k_{(e,e-1)} = 2E_IA_I/(\ell_e + \ell_{e-1})$ and $k_{(e,e+1)} = 2E_IA_I/(\ell_e + \ell_{e+1})$ denoting the stiffness of the segments connecting the elements $e-1$, e and $e+1$, whereas $\mathbf{T} = \mathbf{e}_I\mathbf{e}_I^\mathsf{T}$ denotes the rotation matrix. Substituting relations (54) into the expression of $\Delta\mathbf{F}^e_I$ and setting $k_{(e,e)} = k_{(e,e-1)} + k_{(e,e+1)}$, the assembled stiffness matrices are obtained:

$$\mathbf{K}^\Gamma_{dd} = \mathop{\mathsf{A}}_{e=1}^{n_{en}} \mathbf{K}^e_{dd} \cup \bigcup_{i=e-1}^{e+1} (-1)^{e-i}\, k_{(e,i)} (\mathbf{N}^G_e)^\mathsf{T}\mathbf{T}\,\mathbf{N}^G_i \tag{55}$$

$$\mathbf{K}^\Gamma_{d\alpha} = \mathop{\mathsf{A}}_{e=1}^{n_{en}} \mathbf{K}^e_{d\alpha} \cup \bigcup_{i=e-1}^{e+1} (-1)^{e-i}\, k_{(e,i)} (\mathbf{N}^G_e)^\mathsf{T}\mathbf{T} \tag{56}$$

$$\mathbf{K}^\Gamma_{\alpha d} = \mathop{\mathsf{A}}_{e=1}^{n_{en}} \mathbf{K}^e_{\alpha d} \cup \bigcup_{i=e-1}^{e+1} (-1)^{e-i}\, k_{(e,i)} \mathbf{T}\,\mathbf{N}^G_e \tag{57}$$

$$\mathbf{K}^\Gamma_{\alpha\alpha} = \mathop{\mathsf{A}}_{e=1}^{n_{en}} \mathbf{K}^e_{\alpha\alpha} \cup \bigcup_{i=e-1}^{e+1} (-1)^{e-i}\, k_{(e,i)} \mathbf{T} \tag{58}$$

where n_{en} denotes the number of elements in the enhanced region. With the previous notation, it should be pointed out the for $e = 1$ and $e = n_{en}$ no contribution arises from the elements $e-1$ and $e+1$, respectively. The overall system of equations is therefore written as:

$$\begin{cases} \mathbf{K}^\Gamma_{dd}\mathbf{d} + \mathbf{K}^\Gamma_{d\alpha}\boldsymbol{\alpha} = \mathbf{F}_I + \mathbf{F}_{ext} & \text{(59a)} \\ \mathbf{K}^\Gamma_{\alpha d}\mathbf{d} + \mathbf{K}^\Gamma_{\alpha\alpha}\boldsymbol{\alpha} = \mathbf{P}_I & \text{(59b)} \end{cases}$$

with $\mathbf{F}_{ext} = \mathop{\mathsf{A}}_e \mathbf{F}^e_{ext}$ and the terms $\mathbf{P}_I$ and $\mathbf{F}_I = \mathop{\mathsf{A}}_e \pi^{(e)} \left(\mathbf{N}^G_e\right)^\mathsf{T} \mathbf{P}^e_I$ denoting the contributions to the local and global external force vector, respectively, due to the

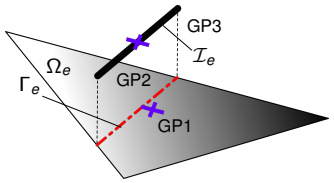

Figure 9: Integration scheme for CST elements.

loads applied at the inclusions ends (see figure 8), with π^e defined as:

$$\pi^e = \begin{cases} 1 & \text{if } \partial\Omega_e \cap \partial_t\Omega \neq \emptyset \\ 0 & \text{otherwise} \end{cases} \tag{60}$$

Static condensation can be applied to system (59), in particular, if we solve equation (59b) with respect to $\boldsymbol{\alpha}$, we have:

$$\boldsymbol{\alpha} = \left(\mathbf{K}^{\Gamma}_{\alpha\alpha}\right)^{-1}\left(\mathbf{P}_I - \mathbf{K}^{\Gamma}_{\alpha d}\mathbf{d}\right) \tag{61}$$

and substituting (61) into equation (59a) yields:

$$\left(\mathbf{K}^{\Gamma}_{dd} - \mathbf{K}^{\Gamma}_{d\alpha}\left(\mathbf{K}^{\Gamma}_{\alpha\alpha}\right)^{-1}\mathbf{K}^{\Gamma}_{\alpha d}\right)\mathbf{d} = \mathbf{F}_I + \mathbf{F}_{ext} - \mathbf{K}^{\Gamma}_{d\alpha}\left(\mathbf{K}^{\Gamma}_{\alpha\alpha}\right)^{-1}\mathbf{P}_I \tag{62}$$

The nodal displacements can therefore be computed as:

$$\mathbf{d} = \left(\tilde{\mathbf{K}}^{\Gamma}_{dd}\right)^{-1}\tilde{\mathbf{F}}^{\Gamma}_{ext} \tag{63}$$

where we have introduced the enriched stiffness matrix and the enriched external force vector:

$$\tilde{\mathbf{K}}^{\Gamma}_{dd} = \mathbf{K}^{\Gamma}_{dd} - \mathbf{K}^{\Gamma}_{d\alpha}\left(\mathbf{K}^{\Gamma}_{\alpha\alpha}\right)^{-1}\mathbf{K}^{\Gamma}_{\alpha d} \tag{64}$$

$$\tilde{\mathbf{F}}^{\Gamma}_{ext} = \mathbf{F}_I + \mathbf{F}_{ext} - \mathbf{K}^{\Gamma}_{d\alpha}\left(\mathbf{K}^{\Gamma}_{\alpha\alpha}\right)^{-1}\mathbf{P}_I \tag{65}$$

Remarks For the sake of simplicity, CST finite elements have been used in the implementation of the numerical model. In such case, matrices $\mathbf{B}_\alpha$ and $\mathbf{B}^*_\alpha$ expressed by relations (33) and (36), respectively, are piece-wise constant, therefore the standard integration rule for linear triangular elements applies for the bulk, with one Gauss-point at the element center of gravity. The contribution of the inclusion is taken into account by means of two additional integration points placed at the segment ends, as depicted in figure 9.

5 Applications

In this section we discuss the numerical validation of the proposed model. The comparison with other modelling strategies is presented, namely the implicit and explicit methods based on standard Galerkin finite elements. Special attention is given to the analysis of the interface behaviour by means of both elementary and full-scale case studies.

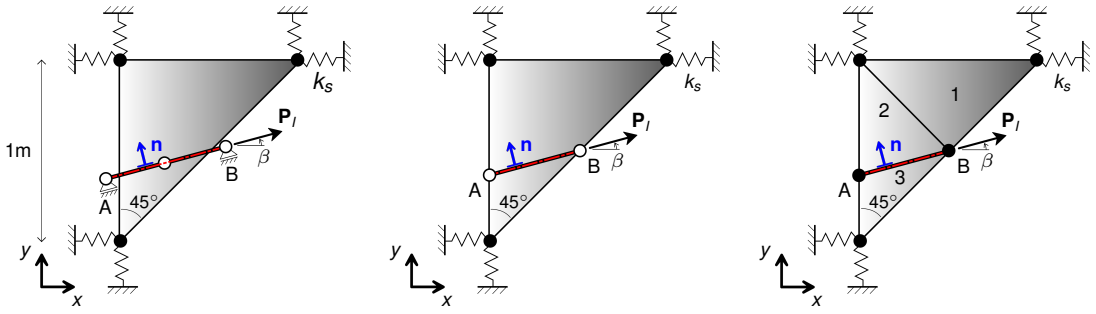

Figure 10: Elementary case study. Enhanced CST model (a), standard CST model (b), reference model (c).

5.1 Elementary example

A concrete structure with an embedded anchor modeled by means of truss finite elements, is submitted to the load $\mathbf{P}_I = P\,\mathbf{e}_I = P\cos\beta\,\mathbf{e}_x + P\sin\beta\,\mathbf{e}_y$, with $P = 10^5\,\mathrm{N}$, applied to the inclusion end, as described in figure 10. Linear springs with stiffness $k_s = 2.36 \times 10^9\,\mathrm{N\,m^{-1}}$ are introduced to represent the interaction with the surrounding domain. We consider for concrete a Young's modulus $E_c = 30\,\mathrm{GPa}$ and a Poisson's ratio $\nu_c = 0.2$. Plane stress conditions are assumed for the computations, with thickness $t = 0.1\,\mathrm{m}$. The effect on the structural response of the inclusion properties (Young's modulus E_I and transversal cross section A_I) as well its inclination β are studied while keeping the load application point fixed. Three approaches are considered as depicted in figure 10. First of all, the enhanced implicit model proposed herein applied to CST elements, then the standard implicit and explicit models (denoted as "standard" and "reference", respectively) based upon regular CST. In the explicit modelling, the domain Ω, discretised into three finite elements, is decomposed into $\Omega^+ = \Omega_1 \cup \Omega_2$ and $\Omega^- \equiv \Omega_3$, while a single finite element is adopted in the implcit modeling. For comparison purposes, in the first case, average local values will be considered for the bulk. In order to represent the inclusion, a two-node linear truss is perfectly bonded to concrete in the models depicted in figures 10b and 10c.

In figure 11 the longitudinal displacement u_s^G at the inclusion center of gravity and the strain energy of concrete are compared for the three modelling strategies. The results are shown for the interval $E_I A_I \in 5 \times [10^7, 10^{10}]$ N in terms of envelope curves. If we assume, for instance, $A_I = 5 \times 10^{-4}\,\mathrm{m^2}$, i.e. $D_I = 2.52 \times 10^{-2}\,\mathrm{m}$ for a circular cross section, such interval corresponds to Young's modulus E_I between $10^2\,\mathrm{GPa}$ and $10^3\,\mathrm{GPa}$. In case of the enhanced model (figure 10a), the inclusion stiffness does not have any influence on the structural behaviour as can be seen from the global equilibrium equation (46) written for the enriched CST:

$$\mathbf{B}^{\mathsf{T}}\boldsymbol{\sigma}^- A^- t + \mathbf{B}^{\mathsf{T}}\boldsymbol{\sigma}^+ A^+ t = (\mathbf{N}^G)^{\mathsf{T}}\,\mathbf{P}_I \tag{66}$$

with $\boldsymbol{\sigma}^- = \boldsymbol{\sigma}_d^- + \boldsymbol{\sigma}_\alpha^-$ and $\boldsymbol{\sigma}^+ = \boldsymbol{\sigma}_d^+ + \boldsymbol{\sigma}_\alpha^+$ as defined in relation (47), whereas the

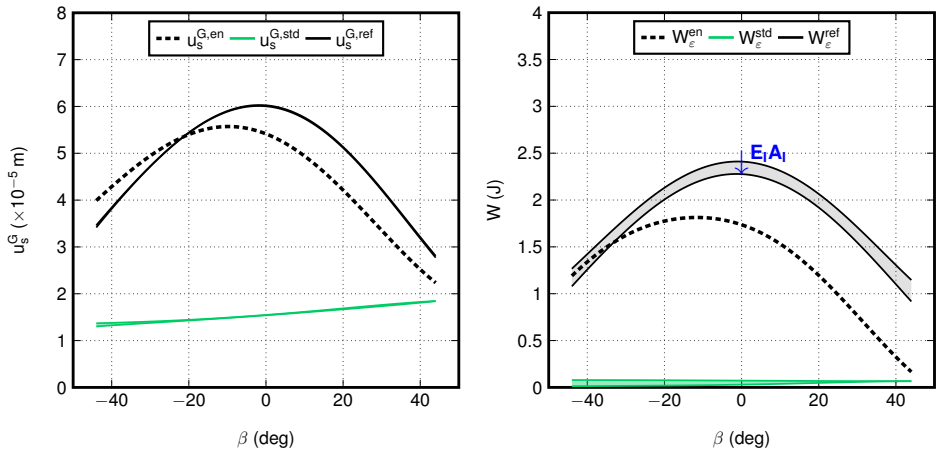

(a) (b)

Figure 11: Longitudinal displacement u_s^G (a) and strain energy W_ε of concrete (b).

local equation (39) becomes:

$$-\ell\, \mathbf{p}^\mathsf{T} [\![\boldsymbol{\sigma}_\alpha]\!]\, t = \mathbf{P}_I \tag{67}$$

being $\boldsymbol{\sigma}_d$ constant all over the element domain and following the reasoning presented in section 2, the identity $\hat{\boldsymbol{\sigma}} \equiv \boldsymbol{\sigma}_\alpha$ can thereby by established. The situation is different for the other strategies (figures 10b and 10c): indeed, since both the truss nodes are linked to concrete, the latter adds a contribution to the overall stiffness matrix. As can be seen in figure 11a, the enhanced formulation improves substantially the overall kinematics of the standard finite element, with a much less stiff behaviour translating in higher strain energy values which are computed as:

$$\begin{aligned} W_\varepsilon &= \frac{1}{2}\int_\Omega \boldsymbol{\varepsilon}^\mathsf{T}\mathbf{D}\boldsymbol{\varepsilon}\,\mathrm{d}V \\ &= \frac{1}{2}\int_\Omega (\bar{\boldsymbol{\varepsilon}}+\hat{\boldsymbol{\varepsilon}})^\mathsf{T}\,\mathbf{D}\,(\bar{\boldsymbol{\varepsilon}}+\hat{\boldsymbol{\varepsilon}})\,\mathrm{d}V \\ &= \frac{1}{2}\left(\overline{W}_\varepsilon + 2\widehat{\overline{W}}_\varepsilon + \widehat{W}_\varepsilon\right) \end{aligned} \tag{68}$$

where the term $\widehat{W}_\varepsilon$ is dominant with respect to the others.

In figure 12 the two contributions $\bar{u}_s^G$ and $\hat{u}_s^G$ expressed by equation (14) are plotted for the enhanced and reference models. Since the single standard CST element is not provided with internal degrees of freedom, in this case we have $\hat{\mathbf{u}}^{\mathrm{std}} = 0$, i.e. $\mathbf{u}^{\mathrm{std}} \equiv \bar{\mathbf{u}}^{\mathrm{std}}$. The respective deformed shapes, shown in figure 13, reveals that the proposed formulation is able to reproduce the major contribution to the overall kinematics given by the longitudinal component $\hat{u}_s^\Gamma$ of the interface displacement $\hat{\mathbf{u}}_\Gamma$. However, from the analysis of figure 13, it appears that there exists a normal component $\hat{u}_\xi^\Gamma$ (much smaller with respect to $\hat{u}_s^\Gamma$) that is not captured by the enhanced model. To check this, it is convenient to switch to the tensor notation and write the

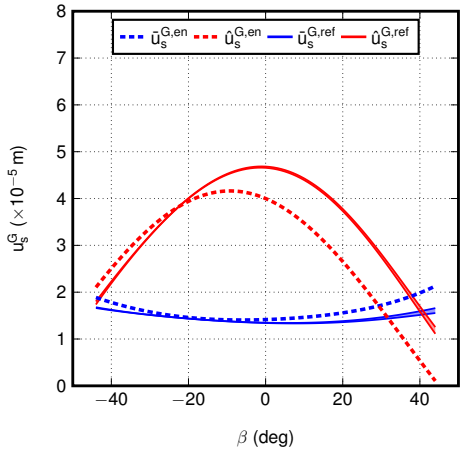

Figure 12: Longitudinal displacement contributions at the inclusion center of gravity.

expression of the stress $\hat{\boldsymbol{\sigma}}$ by computing $\nabla^{\mathrm{s}}\hat{\mathbf{u}} = \nabla^{\mathrm{s}}(\hat{u}_s\mathbf{e}_I + \hat{u}_\xi\mathbf{n})$ with $\hat{u}_s = N_\alpha\alpha_s$ and $\hat{u}_n = N_\alpha\alpha_\xi$, i.e.:

$$\nabla^{\mathrm{s}}\hat{\mathbf{u}} = \left(N_{\alpha,s}\mathbf{e}_I \otimes \mathbf{e}_I + N_{\alpha,\xi}\mathbf{n} \otimes \mathbf{e}_I\right)^{\mathrm{s}} \alpha_s + \left(N_{\alpha,s}\mathbf{e}_I \otimes \mathbf{n} + N_{\alpha,\xi}\mathbf{n} \otimes \mathbf{n}\right)^{\mathrm{s}} \alpha_\xi \tag{69}$$

Being in our case $N^-_{\alpha,s} = N^+_{\alpha,s}$ (see the remarks made in section 3.1), only $N_{\alpha,\xi}$ acts in the computation of the stress jump:

$$[\![\hat{\boldsymbol{\sigma}}]\!] = \mathbb{C}^{\mathrm{ps}} : [\![N_{\alpha,\xi}]\!] \left(\mathbf{n} \otimes \mathbf{e}_I\alpha_s + \mathbf{n} \otimes \mathbf{n}\,\alpha_\xi\right)^{\mathrm{s}} \tag{70}$$

where $\mathbb{C}^{\mathrm{ps}}$ denotes the elasticity tensor in plane stress conditions. The stress vector finally reads:

$$\begin{aligned} \mathbf{n} \cdot [\![\hat{\boldsymbol{\sigma}}]\!] &= [\![N_{\alpha,\xi}]\!] \left(c_{nI}\alpha_s\mathbf{e}_I + c_{nn}\alpha_\xi\mathbf{n}\right) \\ &= [\![N_{\alpha,\xi}]\!] \begin{bmatrix} c_{nI} & 0 \\ 0 & c_{nn} \end{bmatrix} \begin{bmatrix} \alpha_s \\ \alpha_\xi \end{bmatrix} \end{aligned} \tag{71}$$

where $c_{nI} = \mathbf{n}\cdot[\mathbb{C}^{\mathrm{ps}} : (\mathbf{n} \otimes \mathbf{e}_I)^s]\cdot\mathbf{e}_I$ and $c_{nn} = \mathbf{n}\cdot[\mathbb{C}^{\mathrm{ps}} : (\mathbf{n} \otimes \mathbf{n})^s]\cdot\mathbf{n}$ are strictly positive constants. Equation (67) projected in the normal direction $\mathbf{n} = -\sin\beta\,\mathbf{e}_x + \cos\beta\,\mathbf{e}_y$, being $\mathbf{P}_I = P\,\mathbf{e}_I$, finally gives:

$$[\![\sigma_{nn}]\!] = [\![N_{\alpha,\xi}]\!] c_{nn}\alpha_n = 0 \iff \alpha_\xi \equiv \hat{u}^G_\xi = 0 \tag{72}$$

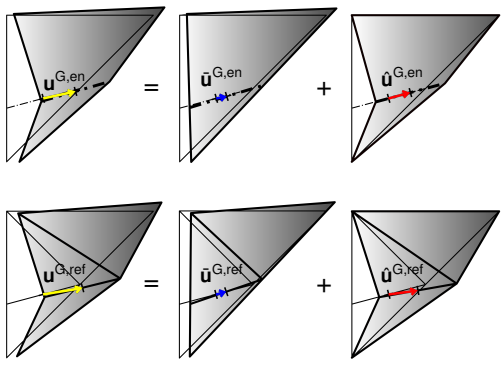

Figure 13: Amplified deformed shapes for $\beta = 15°$ and $E_I A_I = 10^8$ N.

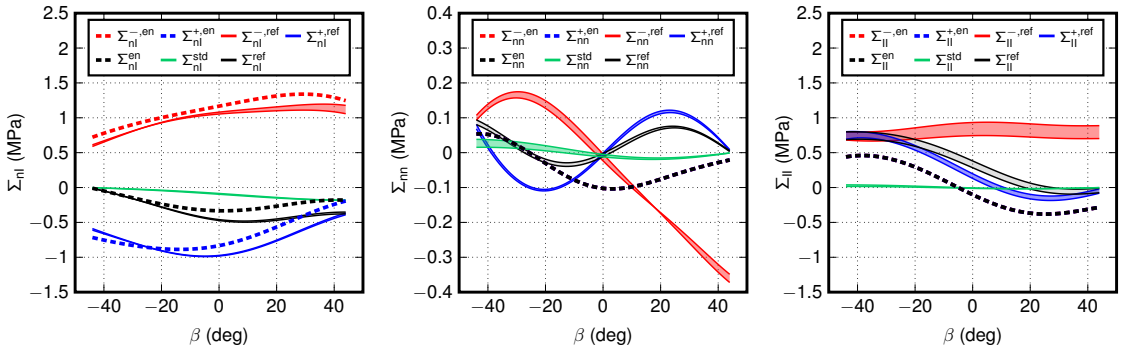

(a) (b) (c)

Figure 14: Tangential stress Σ_{nI} (a), normal stress Σ_{nn} (b) and longitudinal stress Σ_{II} (c) computed in concrete.

Consequently, no coupling between the longitudinal and the normal direction is reproduced by the proposed formulation in case of CST finite elements. Moreover, being $\alpha_\xi = 0$, we also have that the longitudinal stress σ_{II} is continuous across Γ:

$$[\![\sigma_{II}]\!] = [\![N_{\alpha,\xi}]\!] c_{II} \alpha_\xi = 0 \tag{73}$$

with $c_{II} = \mathbf{e}_I \cdot [\mathbb{C}^{\text{ps}} : (\mathbf{n} \otimes \mathbf{n})^s] \cdot \mathbf{e}_I$. On the contrary, since $\alpha_s \neq 0$, a jump arises in the shear stress $\hat{\sigma}_{nI}$ and it is equal to:

$$[\![\hat{\sigma}_{nI}]\!] = [\![N_{\alpha,\xi}]\!] c_{nI} \alpha_s \tag{74}$$

The total stress field is depicted in figure 14 where average values have been considered for the reference simulation ($\boldsymbol{\Sigma}^{\pm,\text{en}} \equiv \boldsymbol{\sigma}^{\pm,\text{en}}$ and $\boldsymbol{\Sigma}^{\pm,\text{std}} \equiv \boldsymbol{\Sigma}^{\text{std}} \equiv \boldsymbol{\sigma}^{\text{std}}$ for the single CST). A good agreement is observed between the simulations, especially the evaluation of the shear stresses is satisfying, with small dependence on the inclusion stiffness which, on the contrary, is more relevant in the computation of the normal stresses (figures 14b and 14c). In figure 15 the interface shear stress (40) is shown.

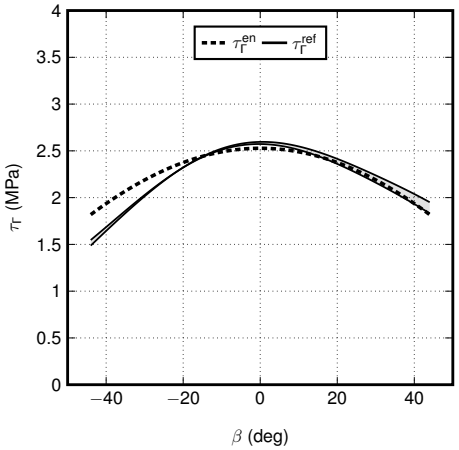

Figure 15: Interface shear stress for $D_I = 2.52 \times 10^{-2}$ m.

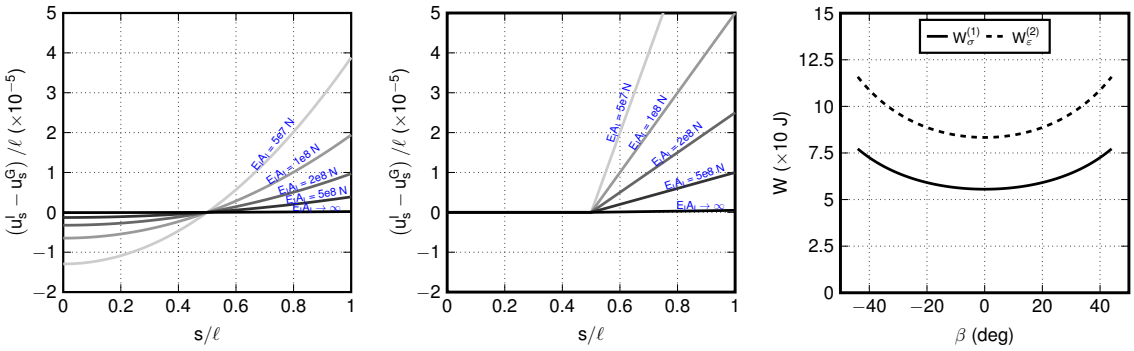

(a) (b) (c)

Figure 16: Local (a) and global (b) normalised longitudinal displacement variation of the inclusion, local complementary strain energy $W_\sigma^{(1)}$ and global strain energy $W_\varepsilon^{(2)}$ for $A_I = 5 \times 10^{-4}\,\mathrm{m}^2$ and $E_I = 300\,\mathrm{GPa}$.

Its expression for a circular cross section reads:

$$\tau_\Gamma = -\frac{[\![\hat{\sigma}_{nI}]\!]}{\pi D_I} t \tag{75}$$

It can be seen that the average interface stress $\tau_\Gamma^{ave} = P/(\pi D_I \ell)$ is exactly evaluated by the proposed formulation, in particular in the present case it is symmetric with respect to the angle β due to the fact that $\ell(\beta) = \ell(-\beta)$, $\forall \beta \in [-45°, 45°]$. Such result is achieved thanks to the fulfilment of the local static equation (67), which is not the case for the reference solution, based on a standard displacement approach. For what concerns the inclusion kinematics, two displacement fields are modeled, a global one which is compatible with the applied Dirichlet boundary conditions (but not with the interface kinematics and stresses) and a local one which is incompatible but statically admissible with respect to the applied loads and the shear stress τ_Γ acting on the lateral surface. The latter can be obtained by integration of the axial strain which, being $\sigma_I = E_I \varepsilon_I$ linear under the constant stress τ_Γ, reads:

$$\begin{aligned} u_s^I &= \int \frac{Ps}{E_I A_I \ell}\,\mathrm{d}s \\ &= \frac{Ps^2}{2E_I A_I \ell} + C \end{aligned} \tag{76}$$

where the static boundary conditions $\sigma_I(0) = 0$ and $\sigma_I(\ell) = P/A_I$ have been imposed. The integration constant C corresponds to a rigid body motion which can be computed by setting $\mathbf{u}_I(\mathbf{x}^G) = \mathbf{u}^G$:

$$C = u_s^G - \frac{P\,\ell}{8 E_I A_I} \tag{77}$$

The displacement fields are shown in figure 16 as well as the complementary strain energy associated to the local displacement field $W_\sigma^{(1)} = P^2\ell/(6\,E_I)$ and the strain energy derived from the global displacement field $W_\varepsilon^{(2)} = P^2\ell/(4\,E_I)$.

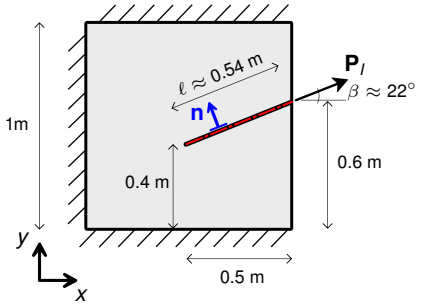

Figure 17: Pull-out test.

The results obtained from this elementary example shows that the enhanced implicit model is suitable for achieving a good accuracy with respect to an explicit approach. The kinematic enrichment allows, indeed, to reproduce the local deformation mode induced by an embedded rod. Both the displacement and strain energy evaluation appears to be significantly improved with respect to the standard CST as well as the static quantites computed at the interface. Moreover, a double kinematic description of the inclusion is achieved by means of a local and global field computed from static and kinematic variables, respectively.

5.2 Structural example

We consider now the generalisation of the elementary case study presented in section 5.1 and representing a pull-out configuration. The material parameters for concrete are kept unchanged, i.e. the Young's modulus $E_c = 30$ GPa and the Poisson's ratio $\nu_c = 0.2$, as well as the thickness $t = 0.1$ m and the applied force $\mathbf{P}_I = P\,\mathbf{e}_I$ with $P = 10^5$ N acting as depicted in figure 17. The Young's modulus of the rod and its transversal cross section are set equal to $E_I = 300$ GPa and $A_I = 5\times10^{-4}\text{m}^2$, respectively. For the latter, a circular shape with diameter $D_I = 2.52 \times 10^{-2}$ m has been assumed. A sensitivity analysis with respect to the spatial discretisation is carried out with focus on the local fields developing in the inclusion and at the interface as well as the convergence properties of the finite element approximation. A CPU time comparison between different approaches is also carried out. For such purposes, unstructured meshes with constant densities have been adopted for the analysis. More efficient strategies could be adopted for the discretisation, such as considering a variable mesh density. This operation would be, however, problem-oriented and difficult to apply in case of several inclusions and more complex reinforcement layouts. In order to keep the analysis as general and objective as possible, such option is not considered here. In the following, we will denote with h_c^{en} the average concrete mesh size and $h_I^{en} = \ell/n_{en}$ the average inclusion size defined by the cutting of the concrete mesh ($h_I^{en} < h_c^{en}$). Four discretisations comprising 4 ($h_I^{en} = 1.35\times10^{-1}$ m), 17 ($h_I^{en} = 3.17\times10^{-2}$ m), 70 ($h_I^{en} = 7.69\times10^{-3}$ m) and 139 ($h_I^{en} = 3.87\times10^{-3}$ m) enhanced elements have been considered for studying the local distributions. The total number of concrete elements is 34 ($h_c^{en} = 2.70 \times 10^{-1}$ m), 508 ($h_c^{en} = 6.75 \times 10^{-2}$ m), 8112 ($h_c^{en} = 1.69 \times 10^{-2}$ m) and 33172 ($h_c^{en} = 8.44 \times 10^{-3}$ m), respectively. The results are therefore compared to the explicit modeling (reference), for which

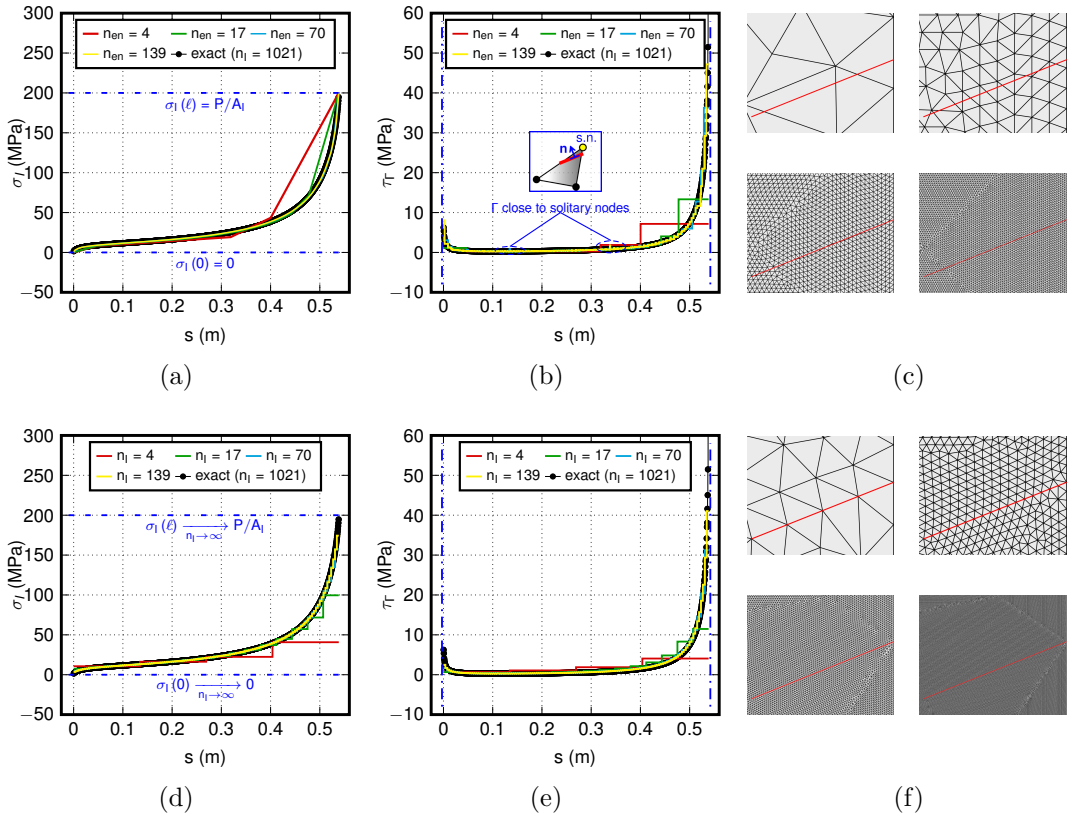

Figure 18: Axial stress σ_I (a), interface shear stress τ_Γ (b) and adopted meshes (c) for the enhanced model. Corresponding distributions (d)-(e) and meshes (f) for the explicit (reference) model.

$h_I^{ref} = \ell/n_I = h_c^{ref}$. In particular, we assume as exact the solution obtained by this latter strategy involving 1021 truss elements at the interface and 8.46×10^6 CST elements for concrete ($h_I^{ref} = h_c^{ref} = 5.27 \times 10^{-4}$ m).

The axial stress and interface stress distributions are shown in figure 18a and 18b for the proposed formulation and in figure 18d and 18e for the explicit model, respectively. In the first case, the evaluation of σ_I seems to be more accurate even for large element sizes, in particular the static boundary conditions at the inclusion ends, i.e. $\sigma_I(0) = 0$ and $\sigma_I(\ell) = P/A_I$, are exactly satisfied. Such fulfilment is therefore independent of the spatial discretisation, whereas their violation is observed (as expected) in figure 18d since they are only asymptotically fulfilled when $n_I \to \infty$. From the analysis of figure 18b, it appears that the stress singularities from the extremities of the inclusion are effectively reproduced. In the same figure, one may also note that, when Γ is close to solitary nodes, the computation of the interface stress may be less accurate. However, such drawback does not appear to affect significantly the axial stress distribution. Indeed, in such circumstances, since the elementary axial force increment $\Delta\mathbf{F}_I$ in equation (39) is proportional to the segment length ℓ_e, such contribution is bounded and does not induce jumps in the overall distribution. An equivalent explanation is that, being τ_Γ related with the

Approach	$n_I = 4$	$n_I = 17$	$n_I = 70$	$n_I = 139$
Enhanced implicit – local	12.89	1.18	0.99	0.51
Enhanced implicit – global	25.33	5.70	0.69	0.42
Explicit	27.97	7.53	1.22	0.44
Implicit	38.60	12.41	2.24	1.39

Table 1: Relative error (%) with respect to the assumed exact solution in the computation of the right end displacement for different modeling approaches.

derivative of σ_I through combination of equations (9) and (19), the first quantity has a lower degree of regularity than the second one and it is consequently more sensitive to the spatial discretisation. In figure 19 we show the local and global longitudinal displacement profiles as described in section 5.1 for the enhanced model, while in figure 19c the results are shown for the explicit model. In the first case, it appears that the displacement at the right end of the inclusion is overestimated for low density values, whereas it is underestimated in the second case. A confirmation of the good performances of the proposed formulation is found by computing the relative errors with respect to such quantity. For the comparison, standard implicit modeling sharing the same concrete mesh of figure 18c but with a uniform inclusion size and all the nodes bonded to concrete (see figure 10b) is also considered. The benefits deriving from the enhanced formulation and the double displacement representation are in this case evident, especially for large mesh sizes. In figure 20 the stresses in the upper and lower concrete layers are shown, as well as the absolute difference around the inclusion with respect to the explicit model for $h_I^{en} = h_I^{ref} = 7.69 \times 10^{-3}$ m ($n_{en} = n_I = 139$). A good agreement is found for σ_{nI} and σ_{nn}, whereas some discrepancy is observed near the ends for σ_{II}. This can be attributed to the different way boundary conditions are applied to the structure (see figure 10).

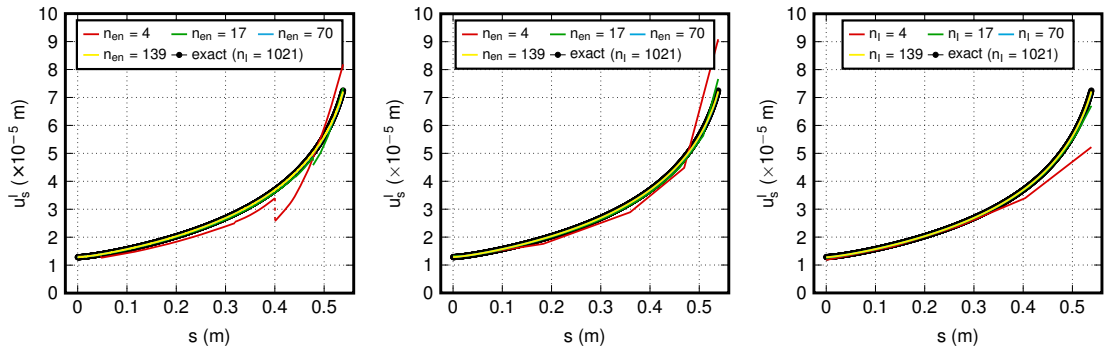

(a) (b) (c)

Figure 19: Local (a) and global (b) longitudinal displacement profiles of the inclusion computed by the enhanced model. Global displacement profile for the explicit model (c).

We now study the convergence properties of the finite element approximation. As for the previous example, three modelling strategies are compared, namely the enhanced implicit model on the one hand, on the other the standard implicit and explicit models based upon regular CST elements. In figure 21 the L_2-norm error of the displacement field defined as

$$\|\boldsymbol{\epsilon}_u\|_{L_2} = \sqrt{\int_\Omega \boldsymbol{\epsilon}_u \cdot \boldsymbol{\epsilon}_u \, \mathrm{d}V} \tag{78}$$

with $\boldsymbol{\epsilon}_u = \mathbf{u} - \mathbf{u}_h$, where $\mathbf{u}$ is the assumed exact solution and $\mathbf{u}_h$ the finite element approximation, and the strain energy norm error

$$\begin{aligned} \|\boldsymbol{\epsilon}_\varepsilon\|_E &= \sqrt{2|W_\varepsilon - W_\varepsilon^h|} \\ &= \sqrt{\int_\Omega \boldsymbol{\epsilon}_{\boldsymbol{\varepsilon}} : \mathbb{C} : \boldsymbol{\epsilon}_{\boldsymbol{\varepsilon}} \, \mathrm{d}V + 2\int_\Omega |\boldsymbol{\epsilon}_{\boldsymbol{\varepsilon}} : \mathbb{C} : \boldsymbol{\varepsilon}_h| \, \mathrm{d}V} \end{aligned} \tag{79}$$

with $\boldsymbol{\epsilon}_{\boldsymbol{\varepsilon}} = \boldsymbol{\varepsilon} - \boldsymbol{\varepsilon}_h$ are plotted for the concrete phase. It should be noted in the previous expression the presence of the term $2\int_\Omega |\boldsymbol{\epsilon}_{\boldsymbol{\varepsilon}} : \mathbb{C} : \boldsymbol{\varepsilon}_h| \, \mathrm{d}V \neq 0$ which corresponds to a violation of the orthogonality condition usually fulfilled by standard Galerkin finite elements. This is attributable to two main factors. On one hand, we compute the interface forces $\mathbf{f}_I$ in equation (24a) from the L_2 projection of the displacement field. On the other hand, the fact that the adopted Petrov-Galerkin approximation

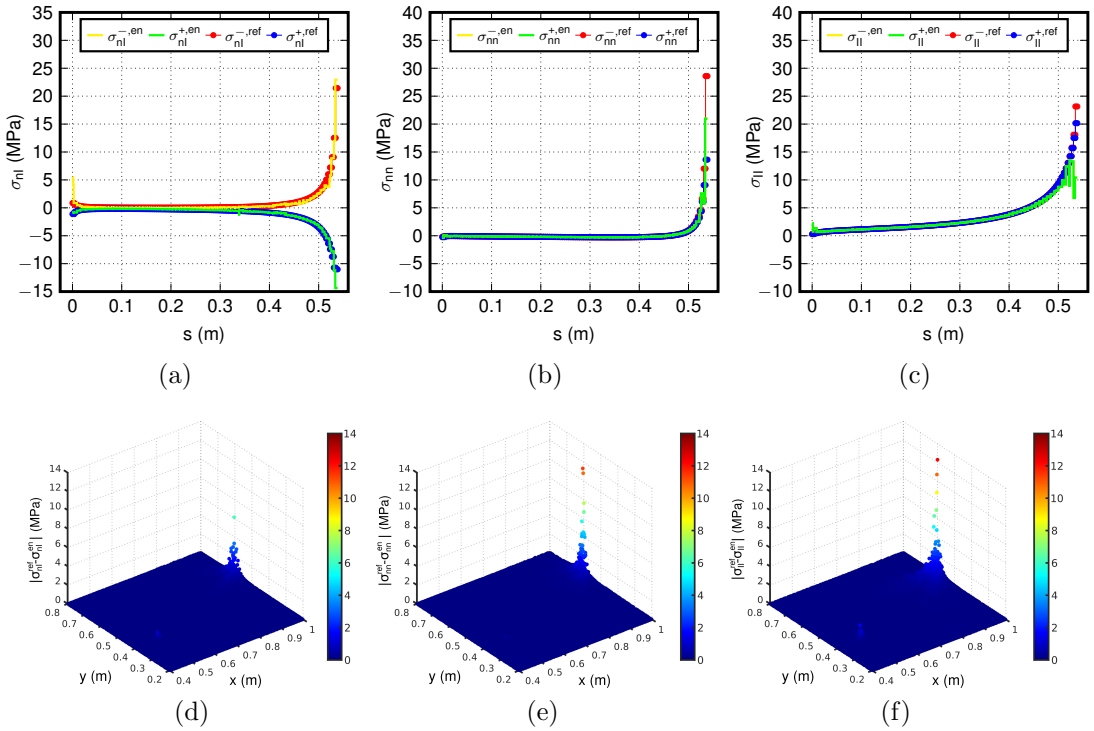

Figure 20: Tangential stress σ_{nI} (a), normal stress σ_{nn} (b) and longitudinal stress σ_{II} (c) in concrete for $h_I^{en} = h_I^{ref} = 7.69 \times 10^{-3}$ m. Absolute differences $|\sigma_{nI}^{ref} - \sigma_{nI}^{en}|$ (d), $|\sigma_{nn}^{ref} - \sigma_{nn}^{en}|$ (e) and $|\sigma_{II}^{ref} - \sigma_{II}^{en}|$ (f).

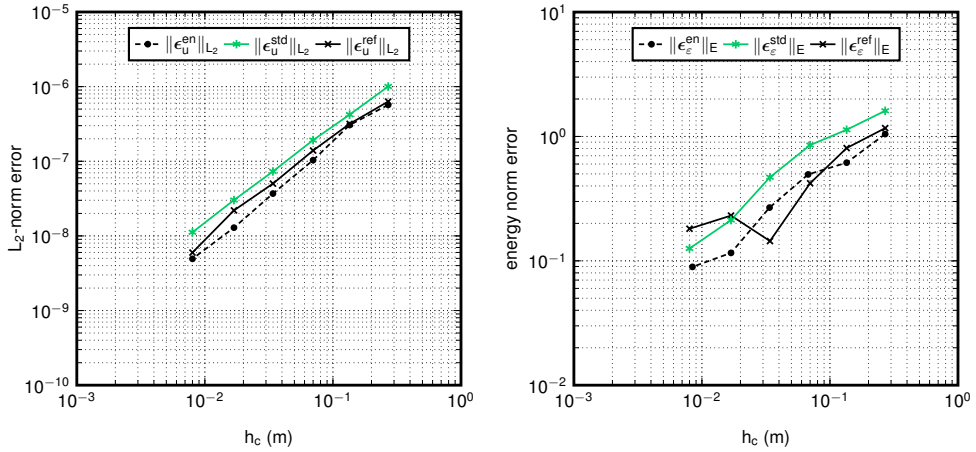

(a) (b)

Figure 21: Convergence curves for concrete with h-refinement. L_2-norm error $\|\boldsymbol{\epsilon}_u\|_{L_2}$ (a) and energy norm error $\|\boldsymbol{\epsilon}_\varepsilon\|_E$ (b).

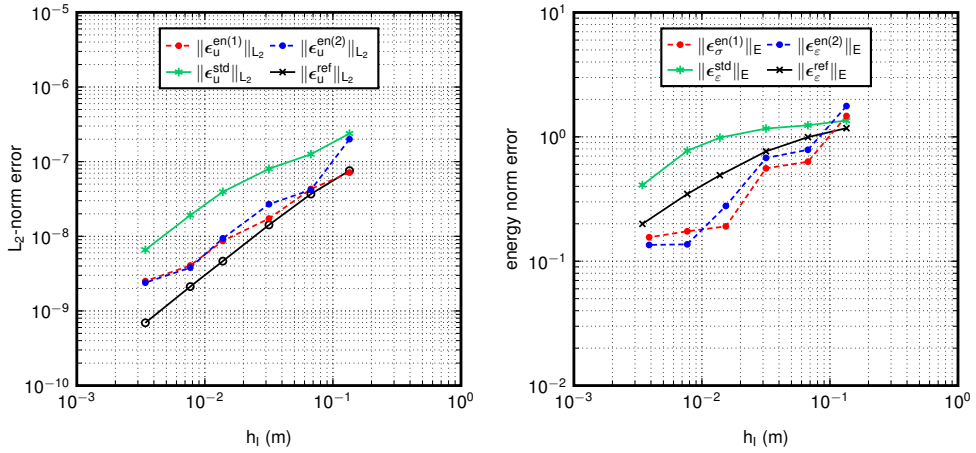

(a) (b)

Figure 22: Convergence curves for the inclusion with h-refinement. L_2-norm error $\|\boldsymbol{\epsilon}_u\|_{L_2}$ (a) and energy norm error $\|\boldsymbol{\epsilon}_{\varepsilon(\sigma)}\|_E$ (b).

corresponds to an oblique projection of the exact solution $\mathbf{u}$ onto the subspace of $\mathbf{u}_h$, translating into the inequality $\mathbf{B}_\alpha^* \neq \mathbf{B}_\alpha$ and the following asymmetry of the global stiffness matrix $(\mathbf{K}_{d\alpha}^e \neq (\mathbf{K}_{\alpha d}^e)^\mathsf{T}$ in definitions (50), (51) and (64)). Hence both for Galerkin and Petrov-Galerkin methods the strain energy error includes the error of the approximation of the boundary condition associated with the interface tractions, i.e. the strain energy convergence will not be necessarily monotonic [57]. Perturbations related with stress singularities are expected as well. In figure 21a it appears that the errors $\|\boldsymbol{\epsilon}_u^{en}\|_{L_2}$ and $\|\boldsymbol{\epsilon}_u^{ref}\|_{L_2}$ converge at similar rates whereas a slightly slower convergence is observed for $\|\boldsymbol{\epsilon}_u^{std}\|_{L_2}$ when $h_c \to 0$. As mentioned above, instabilities occur in the energy norm (see figure 21b), where $\|\boldsymbol{\epsilon}_\varepsilon^{en}\|_E$ shows a stronger convergence with respect to the other methods. The most stable behaviour

is however observed for $\|\boldsymbol{\epsilon}_{\varepsilon}^{std}\|_E$, which can be explained by considering that a stiffer interface reduces the order of the singularity in the finite element solution. The errors for the inclusion are shown in figure 22, where both the local and global kinematics described in section 5.1 have been considered. The best convergence in the L_2 norm is observed in this case for $\|\boldsymbol{\epsilon}_{u}^{ref}\|_{L_2}$. One should not forget, however, that in this case the overall mesh is more refined, being $h_c^{ref} < h_c^{en} = h_c^{std}$. The situation is different for what concerns the energy norms where both $\|\boldsymbol{\epsilon}_{\sigma}^{en(1)}\|_E$ and $\|\boldsymbol{\epsilon}_{\varepsilon}^{en(2)}\|_E$ converge in average faster than the other strategies, despite showing some oscillations. It can be also seen that the convergence of $\|\boldsymbol{\epsilon}_{\varepsilon}^{std}\|_E$ is rather poor up to $h_I \approx 10^{-2}$ m. In case of the enhanced model, the most benefits are observed, in particular, for coarse and intermediate descretisations: indeed, how one would expect from the fulfilment of the patch-test condition (equation (37)), the value of the kinematic enhnancement $\boldsymbol{\alpha}$ goes to zero when the increment $\Delta\mathbf{F}_I$ vanishes. This situation takes place for $h_I \to 0$ as shown in figures 23a and 23b where both the kinematic enhancement and the axial force increment are depicted for the right end element where the load is applied. In order to compare the performance level of the different approaches, in figure 24 we finally plot the reinforcement energy norm error against the CPU time required for the computation, for which $h_c^{en} = h_c^{ref} = h_c^{std}$ has been set. The total number of concrete elements is therefore the same. In this case, the advantages of the enhanced formulation become even more pronounced, in particular, two main observations can be made. First, if we set a constant error value for an intermediate discretisation, the gain in the CPU-time can be estimated being almost one order of magnitude with respect to the other simulations. Second, in the range $t_{\text{CPU}} > 1$ s, the additional time required for solving the enriched problem is only a small portion of the overall computation time. This observation translates into slightly shifted points along the x-axis, whose distance tends to vanish as t_{CPU} increases. To conclude the analyisis, it should be also pointed out that a further time gain is achieved by the implicit approaches with respect to an explicit one in

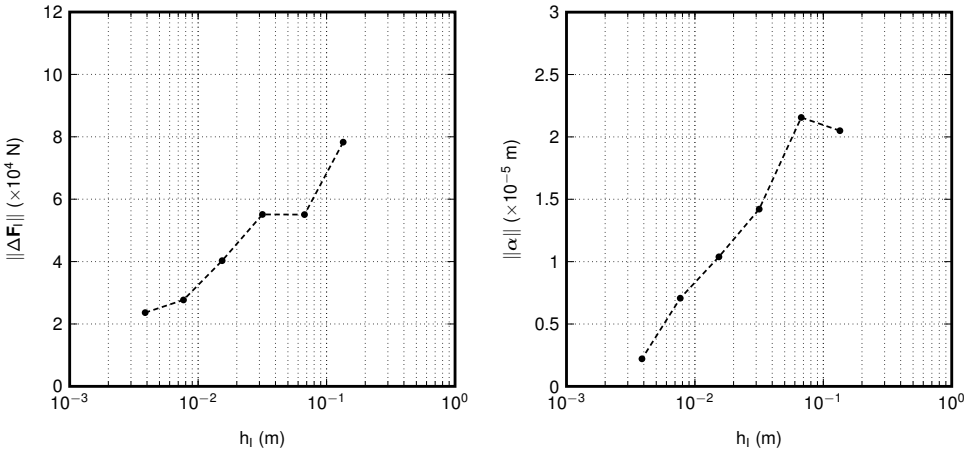

(a) (b)

Figure 23: Axial force increment $\Delta\mathbf{F}_I$ (a) and kinematic enhancement $\boldsymbol{\alpha}$ (b) in the right end element as a function of the average inclusion size h_I.

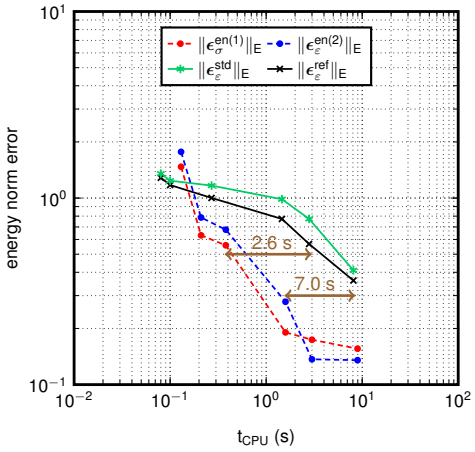

Figure 24: Strain energy norm error as a function of the CPU time.

the realisation of the mesh.

6 Concluding remarks

In this work a new enhanced implicit finite element model has been proposed for simulating the mechanical behaviour of structures with embedded linear inclusions. The considered formulation is based on the enrichment of the macroscopic displacement field through a contribution representing the local kinematics induced by the interaction between the materials. It is shown that the interface forces provoke jumps in the cartesian Cauchy stress tensor computed in the matrix and that such discontinuity can be linked to the average bond stress developing at the inclusion boundary. A non-symmetric Petrov-Galerkin approximation is then derived for the bidimensional case. The main ingredients are the possibility of reproducing the discontinuity in the stress field induced by the heterogeneity and the fulfillement of the patch test ensuring the convergence of the finite element model. A global and local equilibrium equations are thus derived, in particular, the contribution of the inclusion can be modeled at the global level by means of linear trusses, whose action is equilibrated at the local level by the interface tractions computed from the stress field in the bulk. Under the perfect bond assumption, a kinematic relation between the materials is then written in order to reduce the number of unknowns and the overall stiffness matrix and external force vector are derived. Through a static condensation procedure, the nodal displacements are firstly computed, followed by the local enhancements associated with the interface behaviour.

Elementary and structural case studies involving pull-out configurations show that the proposed formulation is able to improve substantially the performances of implicit finite element models based on CST elements and allow to account for the presence of interfaces in a much easier way with respect to standard methods. A good agreement is found with the results given by explicit approaches where the reinforcement layout is considered in the meshing process. A convergence study reveals that the inclusion strain energy computed by the enhanced model converges

in average faster with respect to the other approaches, despite some oscillations that may occur both due to the asymmetric formulation and to the non-uniform finite element decomposition. Such feature does not seem to impact substantially on the evaluation of the main quantities related with the interface and inclusion behaviours. In addition, it has been shown that the overall CPU time for a fixed computation precision in terms of the inclusion strain energy is sensibly reduced.

Further work is required for including bond-slip behaviours and other material nonlinearities.

Acknowledgements

The authors wish to express their most grateful thanks to the French National Research Agency (ANR) for the funding of the ILISBAR project (ANR-16-CE22-0002) by which this study has been carried out.

References

References

[1] W. Koiter, On the diffusion of load from a stiffener into a sheet, The Quarterly Journal of Mechanics and Applied Mathematics 8 (2) (1955) 164–178.

[2] J. D. Eshelby, The determination of the elastic field of an ellipsoidal inclusion, and related problems, Proceedings of the royal society of London. Series A. Mathematical and physical sciences 241 (1226) (1957) 376–396.

[3] E. Brown, The diffusion of load from a stiffener into an infinite elastic sheet, Proceedings of the Royal Society of London. Series A. Mathematical and Physical Sciences 239 (1218) (1957) 296–310.

[4] R. Hill, Elastic properties of reinforced solids: some theoretical principles, Journal of the Mechanics and Physics of Solids 11 (5) (1963) 357–372.

[5] T. Mori, K. Tanaka, Average stress in matrix and average elastic energy of materials with misfitting inclusions, Acta metallurgica 21 (5) (1973) 571–574.

[6] S. Nemat-Nasser, M. Hori, Micromechanics: overall properties of heterogeneous materials, Elsevier, 2013.

[7] T. Clyne, D. Hull, An introduction to composite materials, Cambridge university press, 2019.

[8] B. Sudret, P. de Buhan, Modélisation multiphasique de matériaux renforcés par inclusions linéaires, Comptes Rendus de l'Académie des Sciences-Series IIB-Mechanics-Physics-Astronomy 327 (1) (1999) 7–12.

[9] J. Chen, Z. Yang, G. Holt, Frp or steel plate-to-concrete bonded joints: effect of test methods on experimental bond strength, Steel and Composite Structures 1 (2) (2001) 231–244.

[10] L. De Lorenzis, A. Nanni, Shear strengthening of reinforced concrete beams with near-surface mounted fiber-reinforced polymer rods, Structural Journal 98 (1) (2001) 60–68.

[11] F. Colomb, H. Tobbi, E. Ferrier, P. Hamelin, Seismic retrofit of reinforced concrete short columns by cfrp materials, Composite Structures 82 (4) (2008) 475–487.

[12] S. Qazi, L. Michel, E. Ferrier, Mechanical behaviour of slender rc walls under seismic loading strengthened with externally bonded cfrp, European journal of environmental and civil engineering 17 (6) (2013) 496–506.

[13] F. Ceroni, M. Pecce, S. Matthys, L. Taerwe, Debonding strength and anchorage devices for reinforced concrete elements strengthened with frp sheets, Composites Part B: Engineering 39 (3) (2008) 429–441.

[14] S. T. Smith, Strengthening of concrete, metallic and timber construction materials with frp composites, in: Advances in FRP Composites in Civil Engineering, Springer, 2011, pp. 13–19.

[15] S. T. Smith, S. Hu, S. J. Kim, R. Seracino, Frp-strengthened rc slabs anchored with frp anchors, Engineering Structures 33 (4) (2011) 1075–1087.

[16] R. Sadone, Comportement de poteaux en béton armé renforcés par matériaux composites et soumis à des sollicitations de type sismique et analyse d'éléments de dimensionnement, Ph.D. thesis (2011).

[17] S. Qazi, L. Michel, E. Ferrier, Experimental investigation of cfrp anchorage systems used for strengthening rc joints, Composite Structures 99 (2013) 453–461.

[18] S. Kim, S. T. Smith, Pullout tests on frp anchors, in: Asia-Pacific conference on FRP in structures (APFIS 2007), 2007, pp. 775–82.

[19] T. Ozbakkaloglu, M. Saatcioglu, Tensile behavior of frp anchors in concrete, Journal of Composites for Construction 13 (2) (2009) 82–92.

[20] S. T. Smith, H. Zhang, Z. Wang, Influence of frp anchors on the strength and ductility of frp-strengthened rc slabs, Construction and Building Materials 49 (2013) 998–1012.

[21] L. Contrafatto, M. Cuomo, F. Fazio, An enriched finite element for crack opening and rebar slip in reinforced concrete members, International journal of fracture 178 (1-2) (2012) 33–50.

[22] J. C. Simo, J. Oliver, F. Armero, An analysis of strong discontinuities induced by strain-softening in rate-independent inelastic solids, Computational mechanics 12 (5) (1993) 277–296.

[23] J. Simo, J. Oliver, A new approach to the analysis and simulation of strain softening in solids, Fracture and damage in quasibrittle structures (1994) 25–39.

[24] J. Oliver, M. Cervera, O. Manzoli, Strong discontinuities and continuum plasticity models: the strong discontinuity approach, International journal of plasticity 15 (3) (1999) 319–351.

[25] J. Oliver, A. E. Huespe, M. Pulido, E. Chaves, From continuum mechanics to fracture mechanics: the strong discontinuity approach, Engineering fracture mechanics 69 (2) (2002) 113–136.

[26] E. Car, S. Oller, E. Oñate, An anisotropic elastoplastic constitutive model for large strain analysis of fiber reinforced composite materials, Computer Methods in Applied Mechanics and Engineering 185 (2-4) (2000) 245–277.

[27] F. Rastellini, S. Oller, O. Salomón, E. Oñate, Composite materials non-linear modelling for long fibre-reinforced laminates: Continuum basis, computational aspects and validations, Computers & structures 86 (9) (2008) 879–896.

[28] X. Martinez, S. Oller, F. Rastellini, A. H. Barbat, A numerical procedure simulating rc structures reinforced with frp using the serial/parallel mixing theory, Computers & Structures 86 (15-16) (2008) 1604–1618.

[29] A. Sciegaj, F. Larsson, K. Lundgren, F. Nilenius, K. Runesson, Two-scale finite element modelling of reinforced concrete structures: Effective response and subscale fracture development, International Journal for Numerical Methods in Engineering 114 (10) (2018) 1074–1102.

[30] T. J. Hughes, Multiscale phenomena: Green's functions, the dirichlet-to-neumann formulation, subgrid scale models, bubbles and the origins of stabilized methods, Computer methods in applied mechanics and engineering 127 (1-4) (1995) 387–401.

[31] B. Sudret, Modélisation multiphasique des ouvrages renforcés par inclusions, Ph.D. thesis (1999).

[32] B. Sudret, P. de Buhan, Multiphase model for inclusion-reinforced geostructures: Application to rock-bolted tunnels and piled raft foundations, International Journal for numerical and analytical methods in geomechanics 25 (2) (2001) 155–182.

[33] J. Bleyer, Multiphase continuum models for fiber-reinforced materials, Journal of the Mechanics and Physics of Solids 121 (2018) 198–233.

[34] X. Teng, Y. Zhang, Nonlinear finite element analyses of frp-strengthened reinforced concrete slabs using a new layered composite plate element, Composite Structures 114 (2014) 20–29.

[35] X. Teng, Y. Zhang, X. Lin, Two new composite plate elements with bond–slip effect for nonlinear finite element analyses of frp-strengthened concrete slabs, Computers & Structures 148 (2015) 35–44.

[36] S. Feldfogel, O. Rabinovitch, Full scale analysis of frp strengthened plates with irregular layouts, International Journal of Mechanical Sciences 113 (2016) 239–259.

[37] M. Ben Romdhane, F.-J. Ulm, Computational mechanics of the steel–concrete interface, International journal for numerical and analytical methods in geomechanics 26 (2) (2002) 99–120.

[38] A. Ibrahimbegovic, A. Boulkertous, L. Davenne, D. Brancherie, Modelling of reinforced-concrete structures providing crack-spacing based on x-fem, ed-fem and novel operator split solution procedure, International Journal for Numerical Methods in Engineering 83 (4) (2010) 452–481.

[39] F. Armero, K. Garikipati, An analysis of strong discontinuities in multiplicative finite strain plasticity and their relation with the numerical simulation of strain localization in solids, International Journal of Solids and Structures 33 (20-22) (1996) 2863–2885.

[40] E. Roubin, A. Vallade, N. Benkemoun, J.-B. Colliat, Multi-scale failure of heterogeneous materials: A double kinematics enhancement for embedded finite element method, International Journal of Solids and Structures 52 (2015) 180–196.

[41] T. Belytschko, T. Black, Elastic crack growth in finite elements with minimal remeshing, International journal for numerical methods in engineering 45 (5) (1999) 601–620.

[42] N. Moës, J. Dolbow, T. Belytschko, A finite element method for crack growth without remeshing, International journal for numerical methods in engineering 46 (1) (1999) 131–150.

[43] J. Dolbow, N. Moës, T. Belytschko, Discontinuous enrichment in finite elements with a partition of unity method, Finite elements in analysis and design 36 (3-4) (2000) 235–260.

[44] N. Moës, T. Belytschko, Extended finite element method for cohesive crack growth, Engineering fracture mechanics 69 (7) (2002) 813–833.

[45] T. Rukavina, A. Ibrahimbegovic, I. Kozar, Fiber-reinforced brittle material fracture models capable of capturing a complete set of failure modes including fiber pull-out, Computer Methods in Applied Mechanics and Engineering 355 (2019) 157–192.

[46] F. Radtke, A. Simone, L. Sluys, A partition of unity finite element method for obtaining elastic properties of continua with embedded thin fibres, International Journal for Numerical Methods in Engineering 84 (6) (2010) 708–732.

[47] A. Casanova, L. Jason, L. Davenne, Bond slip model for the simulation of reinforced concrete structures, Engineering Structures 39 (2012) 66–78.

[48] A. Llau, L. Jason, F. Dufour, J. Baroth, Finite element modelling of 1d steel components in reinforced and prestressed concrete structures, Engineering Structures 127 (2016) 769–783.

[49] H. Vincent, M. Arquier, J. Bleyer, P. de Buhan, Yield design-based numerical analysis of three-dimensional reinforced concrete structures, International Journal for Numerical and Analytical Methods in Geomechanics 42 (18) (2018) 2177–2192.

[50] L. Dormieux, D. Kondo, F.-J. Ulm, Microporomechanics, John Wiley & Sons, 2006.

[51] A. N. Brooks, T. J. Hughes, Streamline upwind/petrov-galerkin formulations for convection dominated flows with particular emphasis on the incompressible navier-stokes equations, Computer methods in applied mechanics and engineering 32 (1-3) (1982) 199–259.

[52] J. Reddy, An introduction to the finite element method, Vol. 1221, McGraw-Hill New York, 2004.

[53] M. Jirásek, Comparative study on finite elements with embedded discontinuities, Computer methods in applied mechanics and engineering 188 (1-3) (2000) 307–330.

[54] P. Wriggers, Nonlinear finite element methods, Springer Science & Business Media, 2008.

[55] A. Ibrahimbegovic, Nonlinear solid mechanics: theoretical formulations and finite element solution methods, Vol. 160, Springer Science & Business Media, 2009.

[56] R. De Borst, M. A. Crisfield, J. J. Remmers, C. V. Verhoosel, Nonlinear finite element analysis of solids and structures, John Wiley & Sons, 2012.

[57] H.-S. Oh, I. Babu, et al., The method of auxiliary mapping for the finite element solutions of elasticity problems containing singularities, Journal of Computational Physics 121 (2) (1995) 193–212.